*J. Fluid Mech.* (2001), *vol.* 434, *pp.* 209–241. Printed in the United Kingdom

# Shear layers driven by turbulent plumes

By A. B. D. WONG, R. W. GRIFFITHS AND G. O. HUGHES
Research School of Earth Sciences, The Australian National University, Canberra,
ACT 0200, Australia

(Received 12 March 1998 and in revised form 14 October 2000)

A turbulent plume from a continuous source of buoyancy in a long tank is shown to generate a series of quasi-steady counterflowing horizontal shear layers throughout the tank. Both the horizontal flow velocity and the depth of the shear layers are observed to decrease with distance above/below the plume outflow. The shear layers are supported by the stable density stratification produced by the plume and are superimposed on the vertical advection and entrainment inflow that make up the so-called 'filling box' circulation. Thus, at some depths, the surrounding water flows away from the plume instead of being entrained, although we see no evidence of 'detrainment' of dense plume water. Given the stratification produced by the plume at large times, the timescale for the velocity structure to adjust to changes in forcing is proportional to the time for long internal gravity waves to travel the length of the tank. The shear layers are interpreted in terms of internal normal modes that are excited by, and which in turn determine, the horizontal plume outflow. The sixth and seventh baroclinic modes typically dominate because at the level of the plume outflow their phase speed is approximately equal and opposite to the vertical advection in the 'filling box'. Also, the approximate balance between phase speed and advection is found to hold throughout the tank, resulting in the observed quasi-steady flow structure. Viscosity causes the horizontal velocity in the shear layers to decrease with distance above/below the plume outflow, and is thought to be responsible for a low-frequency oscillation in the flow structure that is observed during experiments.

## 1. Introduction

Most studies of turbulent buoyant plumes have focused on the plume flow itself, with relatively little attention being paid to associated motions in the fluid surrounding the plume. Morton, Taylor & Turner (1956) first formulated a model for plumes based on Taylor's entrainment hypothesis (Turner 1997) and quantified the radius, velocity and density of the plume as functions of vertical distance from the source. They also determined the effect a stratified environment has on the height reached by a rising plume. Baines & Turner (1969) noted that, in this description, it is implicitly assumed that the environment is infinite so that the density distribution can be specified in advance and does not change during the period of interest. However, when a plume falls into surroundings of finite volume, such as a laboratory tank or ocean basin, the plume modifies its environment and the problem becomes time-dependent. Baines & Turner (1969) gave solutions for the large-time steady-state flow in which the outflow from a descending plume generates a relatively slow upwards motion in the environment and establishes a stable stratification. Entrainment into the plume was assumed to draw water towards the plume at all depths above the outflow at a rate given by the 'entrainment assumption'. The outflow layer from the plume source at the bottom (or top in the case of a less dense plume) has been found to occupy a quarter of the water depth (Manins 1979). The evolution of the stratification has also been studied by Germeles (1975) and Worster & Huppert (1982). This ‘filling box’ model with various modifications has since been employed in many studies including the filling of containers of liquefied natural gas (Germeles 1975), turbulent flows down sloping boundaries in the oceans (Killworth 1977), the effects of time-dependent plume fluxes on production of ocean bottom waters (Killworth & Turner 1982), development of stratification in magma chambers (Turner 1980) and ventilation in buildings (Cooper & Linden 1966; Linden & Cooper 1996).

The ‘filling box’ process has generally been studied in boxes having lengths and widths comparable to the water depth, and the theoretical analysis has assumed motions outside the plume to be small. In this paper, we report experiments which show that in long tanks a series of strong counterflowing shear layers is established in the stratification produced by the ‘filling box’ mechanism. We present evidence that the layers are produced by internal gravity wave normal modes excited by the plume outflow. They are similar in nature to columnar modes generated by internal intrusions into density gradients (Manins 1976) or the slow horizontal motion of obstacles in density gradients (Bretherton 1967). In § 2, we recall the theoretical velocities and stratification given by the ‘filling box’ solution of Baines & Turner (1969). Our experiments are described in § 3 and our observations and results are given in § 4. Comparisons with theoretical solutions for the normal modes and with other systems that show related flow structures are given in § 5 followed by conclusions in § 6.

## 2. The ‘filling box’ solution

The analytical solutions of Baines & Turner (1969) predicting the properties of a buoyant plume and the density stratification produced in a finite environment are reproduced here. The reader is referred to Baines & Turner (1969) for full details, but we will need some of the analytical results for comparison with our observations and for calculation of the baroclinic normal modes.

For the ‘filling box’ analysis we assume that buoyancy-driven convection is the dominant transport mechanism in the plume, whereas, far away from the plume, the only motions are those of passive advection. Manins (1979) has noted that in boxes of small aspect ratio (length/depth $< 1.2$) an inertial overturning motion is set up by the plume which mixes the environment water from top to bottom. We consider only much longer boxes. We also assume that the smallest horizontal dimension of the tank is larger than the diameter of the plume at the bottom so that the plume does not interact with the sidewalls of the tank.

During its descent, the dense plume entrains surrounding water and therefore increases in radius and decreases in density. The first plume water to reach the bottom spreads in an outflow layer, the top of which forms the ‘first front’ (a discontinuity in density separating the overlying homogeneous water from water that has passed through the plume). At later times, the plume entrains some of the dense water from below the first front, making the outflow progressively denser. This generates a vertical advection throughout the environment; the first front is therefore lifted upwards and a stable stratification is established.

Let $\rho_p$, $R$ and $W$ be the density, radius and vertical (downward) velocity of the plume, respectively, $\rho_e$ the density of the surrounding water, $\rho_r$ a reference density (taken to be that of the environment water at the source level) and $V$ the vertical velocity in the environment, with $t$ the time and $y$ the vertical coordinate. We assume a top-hat profile in which the plume properties are constant across a horizontal cross-section. The equations representing the conservation of volume, momentum and mass deficiency are

$$\left.\begin{aligned} \frac{\partial}{\partial y}(\pi R^2 W) &= 2\pi E R W, \\ \frac{\partial}{\partial y}(\pi R^2 W^2 \rho_p) &= \pi R^2 g(\rho_p - \rho_e), \\ \frac{\partial}{\partial y}[\pi R^2 W(\rho_p - \rho_r)] &= 2\pi E R W(\rho_e - \rho_r), \end{aligned}\right\} \tag{1}$$

while equations representing conservation of volume and density in the environment are

$$\left.\begin{aligned} AV &= -\pi R^2 W, \\ \frac{\partial}{\partial t}\left(g\frac{\rho_e - \rho_r}{\rho_r}\right) &= V\frac{\partial}{\partial y}\left(g\frac{\rho_e - \rho_r}{\rho_r}\right). \end{aligned}\right\} \tag{2}$$

Here, $E$ is the experimentally determined entrainment coefficient (Turner 1986), $g$ is the acceleration due to gravity and $A$ is the horizontal cross-sectional area of the box.

The non-dimensionalization scheme employed to reduce equations (1) and (2) to the simplest form for analysis is

$$\left.\begin{aligned} &y = H\zeta, \quad t = 2^{-4/3}E^{-4/3}\pi^{-2/3}AH^{-2/3}F^{-1/3}\tau, \\ &R = 2EHr, \quad W = 2^{-2/3}E^{-2/3}\pi^{-1/3}H^{-1/3}F^{1/3}w, \\ &g\frac{\rho_p - \rho_r}{\rho_r} = 2^{-4/3}E^{-4/3}\pi^{-2/3}H^{-5/3}F^{2/3}f_p, \\ &g\frac{\rho_e - \rho_r}{\rho_r} = 2^{-4/3}E^{-4/3}\pi^{-2/3}H^{-5/3}F^{2/3}f_e, \\ &V = 2^{4/3}E^{4/3}\pi^{2/3}H^{5/3}F^{1/3}A^{-1}v, \end{aligned}\right\} \tag{3}$$

where $H$ is the effective height of the buoyancy source (see Baines & Turner 1969) and $F = \pi R^2 W g(\rho_p - \rho_e)/\rho_r$ is the buoyancy flux from the source at $y = 0$.

After using (3) to scale (1) and (2), we obtain the same dimensionless equations that Baines & Turner (1969) solved. They found a power series solution for asymptotically large times when the plume radius, vertical velocity and density anomaly relative to the environment no longer vary with time at a given depth, but the plume and environment densities increase linearly in time at all depths. Taking a (virtual) point source at $\zeta = 0$, the solution (to three terms) is

$$r^2 w\,(= -v) = 0.460\zeta^{5/3} - 0.0588\zeta^{8/3} - 0.0100\zeta^{11/3}, \tag{4a}$$

$$rw = 0.766\zeta^{2/3} - 0.157\zeta^{5/3} - 0.0366\zeta^{8/3}, \tag{4b}$$

$$f_e = -\zeta^{-2/3}(3.27 - 0.837\zeta - 0.0623\zeta^2) + c, \tag{4c}$$

$$f_p = f_e + (\zeta - 1)/v. \tag{4d}$$

Equation (4$c$) describes the functional dependence of the environment buoyancy $f_e$ on depth and since $f_e$ depends on how much buoyancy has been added to the system, the equation involves a term $c$ that is linearly dependent on $\tau$. The dependence on $\tau$ can be eliminated if we consider $f_e^*(\zeta) = f_e(\tau, \zeta) - f_e(\tau)_{\zeta=1}$, that is, a buoyancy deficit compared to the bottom that gives $f_e^* = 0$ at $\zeta = 1$. Plots of the plume properties

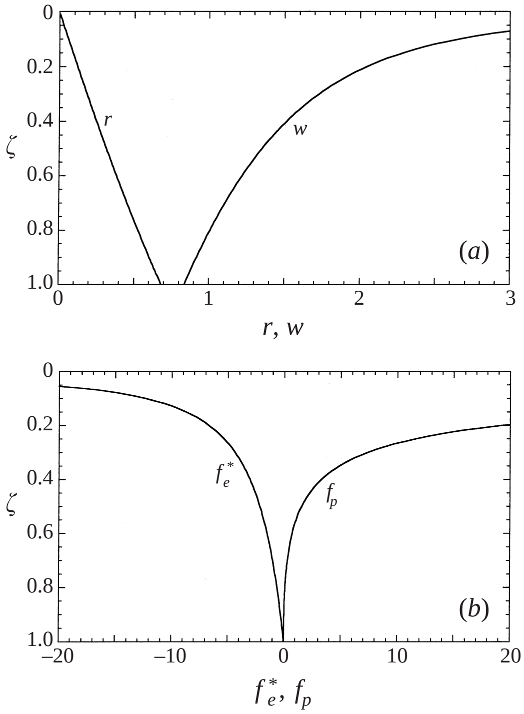

FIGURE 1. The theoretical solution in the asymptotic case given by (4): (*a*) plume radius $r$ and vertical velocity $w$ and (*b*) plume buoyancy $f_p$ and environment buoyancy $f_e^*$ relative to the bottom of the tank. As $\zeta \to 0$, $f_p \to \infty$ and $f_e^* \to -\infty$.

given by (4) and $f_e^*$ are shown in figure 1. Baines & Turner (1969) also described experiments that confirm these theoretical solutions.

In the solution (equation (4)), the entrainment volume per unit depth into the plume is assumed to be $2\pi REW$ at all depths. For an axisymmetric plume far from all sidewalls, this provides us with the horizontal velocity directed radially into the plume. In the experiments reported below, the plume is also placed near one end of a long channel in order to constrain the flow in the environment far from the plume to be two-dimensional. (Experiments indicate that the flow in the environment is approximately two-dimensional at a distance of about two plume radii from the axis of the plume.) We assume that the entrained water is sourced evenly across the horizontal cross-section of the tank so that the horizontal volume transport increases linearly from zero at the end of the tank opposite the plume to $2\pi REW$ at the edge of the plume. Thus, if $B$ and $L$ are the width and length of the tank, respectively, and $x$ the distance from the plume, then the horizontal velocity $U_e$ attributed to entrainment is

$$U_e = -2\pi ERW \frac{(L-x)}{BL}. \tag{5}$$

(The negative sign indicates that entrainment velocities are directed towards the plume.) The scaling between $U_e$ and its dimensionless equivalent $u_e = -rw$ can be calculated as

$$U_e = 2^{4/3}\pi^{2/3}E^{4/3}F^{1/3}H^{2/3}B^{-1}L^{-1}(L-x)u_e. \tag{6}$$

The dimensionless inflow velocity $u_e$ is plotted in figure 2.

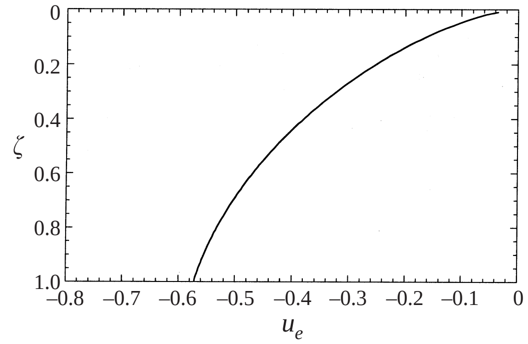

FIGURE 2. The far-field horizontal velocity given by (6) and induced by entrainment into a plume under the assumption of a dynamically passive environment in the 'filling box' model. Negative values of $u_e$ indicate velocity towards the plume.

## 3. Experiments

In the experiments, a dense salt solution was released at a steady rate through a small nozzle protruding just below the free surface of a tank of water. The nozzle, about 6 mm in diameter, was wide enough to ensure that the velocity and momentum of the released water was small, so that the source approximated a pure buoyancy source. The nozzle was positioned near one end of the tank and equidistant from three sidewalls. A peristaltic pump maintained a constant flux of salt water through the nozzle. A typical flow rate used in the experiments was $3.85 \times 10^{-7}\,\mathrm{m^3\,s^{-1}}(= 0.385\,\mathrm{cm^3\,s^{-1}})$ with salt solution densities ranging from 1090 to $1180\,\mathrm{kg\,m^{-3}}$.

Two tanks were used. The first was 1.1 m long, 0.3 m wide and 0.24 m deep whereas the second was 2.0 m long, 0.2 m wide and 0.4 m deep. The nozzles were positioned in the vertical to give effective depths of 0.16 m and 0.235 m in both tanks and, additionally, 0.3 m and 0.38 m in the larger tank.

Horizontal velocities far from the plume were measured by dropping crystals of potassium permanganate into the tank. As the crystals descended to the bottom, they dissolved to produce a vertical dye line. Horizontal velocities were calculated by measuring the distortion of this dye line in a short period of time. The short time interval was crucial for minimizing both the influence of the endwalls and the errors due to simultaneous upwelling of the water. The movement of the dye line was recorded on video. A grid of lines with 1 cm spacing on the front of the tank allowed measurements of dye displacement correct to 0.5 cm from the video recording.

Conductivity profiles and time records at a fixed point were measured by a four-wire conductivity probe (MSCI 5201, Precision Measurement Engineering, USA). Simultaneous thermistor measurements (GB38P12, Fenwal Electronics, USA) provided a temperature correction for the conversion of conductivity to density using the equations of Ruddick & Shirtcliffe (1979). Fractional density changes of less than $10^{-7}$ could be detected.

We conducted 12 experiments, all starting with tanks containing homogeneous fluid. The parameters for these experiments are given in table 1 along with three timescales: $\overline{N^{-1}}$ (where $\overline{N^{-1}}$ is the depth-averaged inverse buoyancy frequency at large times), $t_w = \overline{N^{-1}}(L/H)$, the timescale for long waves to travel the length of the tank, and $t_a = 33.7A/H^{2/3}F^{1/3}$, the time for vertical advection of water in the 'filling box' environment. The advection time is derived from the non-dimensionalization for $t$

used in (3), and is the time predicted by the theory for the first front to reach $\zeta = 0.1$. Some of the 12 experiments were used to reveal the horizontal velocity structure at large times; these will be discussed in § 4.1. All experiments were used to measure the long period oscillations in the density at a fixed point in the tank and also the development of shear layers in a pre-stratified tank. This was accomplished by running the plume for up to 4 h. Within the first hour, the first front approached the level of the source and the density profile approached the asymptotic shape. Conductivity profiles at a fixed value of $x$ were taken both before and after the asymptotic state had been reached. We will see in § 4.2 that oscillations in the conductivity profiles correspond to changes in the horizontal velocity structure. After conductivity profiles had been taken, the plume was turned off and motions in the stratified tank were allowed to settle to rest. The plume was then restarted and the subsequent redevelopment of the horizontal velocity profile monitored (§ 4.3).

The entrainment constant $E$ was measured by comparing the progress of the first front with the analytical solution of Baines & Turner (1969). The value that we use is $E = 0.129$. Since the entrainment constants for 'top-hat' and Gaussian profiles differ by a factor of $\sqrt{2}$ (see Turner 1973, 1986), our entrainment constant corresponds to 0.0912 for a Gaussian profile, and is therefore consistent with those used in other studies.

## 4. Results

### 4.1. *The circulation*

The most striking observation was that the stratified environment produced by a turbulent plume supported a strong and persistent series of layers. These layers appeared as dominant features in the profiles of horizontal velocity, as seen in figure 3(*a*), but corresponded to extremely small perturbations in the density gradient. Hence, we call these 'shear layers' in order to distinguish them from density layering. Figure 4 shows characteristic horizontal velocity profiles halfway along the tank in three experiments. The measured velocities are normalized using the scale given in (6) for the entrainment velocity $u_e$. At the bottom of the tank, the outflow-layer thickness was approximately a quarter of the tank depth. Immediately above the outflow layer, there was a layer of similar thickness moving towards the plume. In the upper half of the tank there were several layers. Both vertical scales and the magnitudes of the horizontal velocities in the shear layers generally decreased with height. The local velocity extrema at the centre of the third and fifth layers from the bottom were almost zero, corresponding to near stationary water. Between these two layers, there was a region of moderate flow towards the plume. At the third velocity extremum ($\zeta = 0.3$–$0.4$), the velocity oscillated slowly from positive to negative, so that the flow was at times away from the plume. A streak photograph (figure 3*b*) not only shows the shear layers, but also indicates that the horizontal velocities heading towards the plume decrease with increasing horizontal distance from the plume. Eddies, which are the result of residual turbulence in the plume outflow, are also seen in the photograph.

Another view of this previously unexpected velocity structure is obtained by subtracting the predicted horizontal inflow velocity due to entrainment from the measured velocity (figure 4*b*). Layers can be defined as those regions of the flow lying between zero crossings in the vertical profile of the horizontal velocity difference $u - u_e$.

At the end of the tank away from the plume, we also observed a concentrated upward flow from the bottom outflow layer that fed the return flow towards the plume

| | Experiment parameters | | Timescales | | | Results | | |
|---|---|---|---|---|---|---|---|---|
| Number | Tank dimensions $L \times B \times H$ (m) | Buoyancy flux ($10^{-7}$m$^4$ s$^{-3}$) | $\overline{N^{-1}}$ (s) | $\overline{N^{-1}}(L/H)$ $t_w$(s) | $33.7A/H^{2/3}F^{1/3}$ $t_a$(s) | Time for layers to develop $t_e$(s) | Oscillation period of layers $t_o$(s) | Predicted vertical wavenumber $m(0)H$ |
| 1 | 2.0 × 0.2 × 0.16 | 6.81 | 2.05 | 25.6 | 5200 | 300 ± 60 | 1620 ± 120 | 8.8 |
| 2 | 2.0 × 0.2 × 0.235 | 6.81 | 3.42 | 29.1 | 4030 | 360 ± 60 | 2040 ± 120 | 7.2 |
| 3 | 2.0 × 0.2 × 0.30 | 6.81 | 4.74 | 31.6 | 3420 | 420 ± 60 | 2280 ± 60 | 6.4 |
| 4 | 2.0 × 0.2 × 0.38 | 6.81 | 6.50 | 34.2 | 2910 | 480 ± 60 | 2640 ± 60 | 5.7 |
| 5 | 2.0 × 0.2 × 0.16 | 3.34 | 2.60 | 32.5 | 6600 | 360 ± 60 | 2220 ± 60 | 8.8 |
| 6 | 2.0 × 0.2 × 0.235 | 3.34 | 4.34 | 36.9 | 5100 | 480 ± 60 | 2010 ± 90 | 7.2 |
| 7 | 2.0 × 0.2 × 0.30 | 3.34 | 6.01 | 40.1 | 4330 | 450 ± 60 | 2280 ± 60 | 6.4 |
| 8 | 2.0 × 0.2 × 0.38 | 3.34 | 8.24 | 43.4 | 3700 | 600 ± 60 | 2280 ± 60 | 5.7 |
| 9 | 1.1 × 0.3 × 0.16 | 6.81 | 2.05 | 14.1 | 4290 | 150 ± 30 | 2400 ± 300 | 10.7 |
| 10 | 1.1 × 0.3 × 0.235 | 6.81 | 3.42 | 16.0 | 3320 | 180 ± 30 | 2430 ± 270 | 8.8 |
| 11 | 1.1 × 0.3 × 0.16 | 3.34 | 2.60 | 17.9 | 5440 | 180 ± 30 | 2190 ± 210 | 10.7 |
| 12 | 1.1 × 0.3 × 0.235 | 3.34 | 4.34 | 20.3 | 4210 | 210 ± 30 | 2130 ± 60 | 8.8 |

TABLE 1. Parameters and results for the experiments.

(*a*)

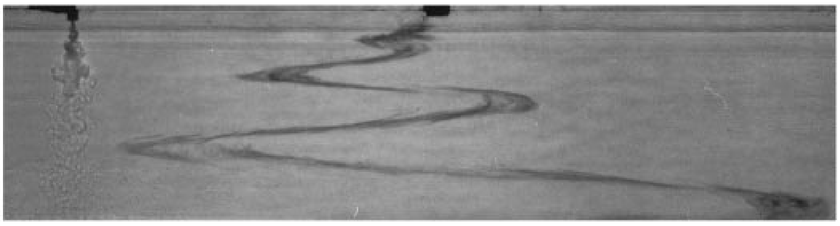

(*b*)

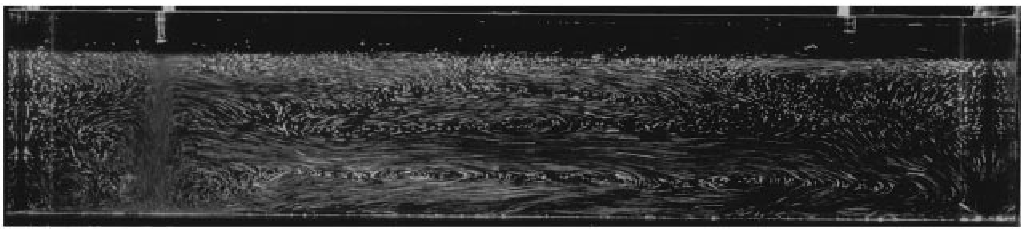

FIGURE 3. (*a*) A photograph of a typical experiment (in a 1.1 m tank). Potassium permanganate crystals dropped into the tank left an initially vertical line of dissolved dye in the water. As this dye line moved passively in the water, it revealed the shear layers generated by the plume outflow. The tracer was also used to measure the horizontal velocities. (*b*) A streak photograph of a typical experiment.

in the second layer. This existed because the uniform vertical advection distributed over the area of the box at the top of the outflow layer was insufficient to accommodate the total volume flux supplied to the layer by the turbulent plume. The same process continued to operate to some extent above the second shear layer with a tendency for a part of the horizontal volume flux in each layer to be directed by the endwalls to a return flow in the next layer.

It should be emphasized that parcels of water did not necessarily traverse the tank from end to end during their residence time in each layer. The distributed vertical advection of water ‘short-circuited’ the paths. For example, there was little horizontal flow (relative to the tank) in the third layer, yet a thin horizontal layer of dyed water was seen to migrate upwards through this shear layer. Thus, those parcels of water which were not entrained into the plume migrated upwards through the series of shear layers, experiencing an oscillatory horizontal velocity.

### 4.2. *Long period oscillations*

At large times after the stratification had developed, the system did not reach a steady state, but instead continued to support slow oscillations. As the first front approached $\zeta = 0.1$, the number of shear layers oscillated between four and five. When the first front had later reached $\zeta = 0.05$, the number of layers oscillated between five and six. The maximum number of layers typically observed was six, however, seven layers were observed in a rare instance. The horizontal velocity profiles obtained during a fluctuation from five to four layers and back are shown in figure 5. The velocities are again normalized using the scale given in (6).

Velocity fluctuations (corresponding to the changing number of layers), were most visible in the region $0.15 < \zeta < 0.45$. At these depths, the positions of the extrema in horizontal velocity shifted, resulting in large velocity fluctuations at a given depth.

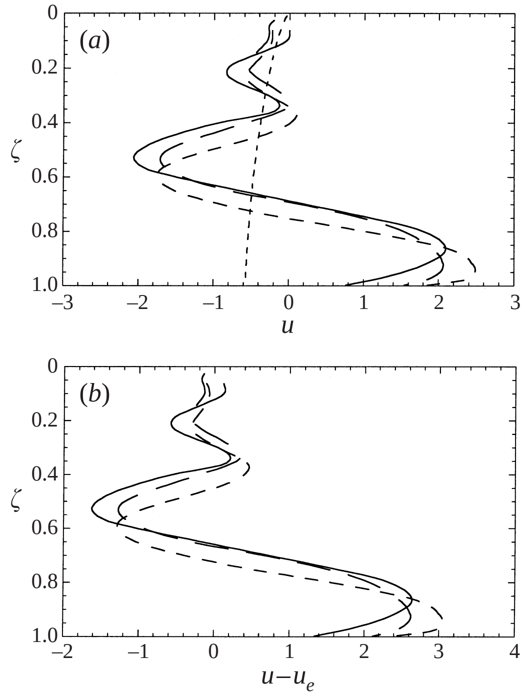

FIGURE 4. Sample horizontal velocity profiles measured halfway along the tank in three experiments listed in table 1: ——, experiment 10; — —, experiment 4; – – – –, experiment 2. (*a*) The measured velocities $u$ contrasted with - - -, the predicted two-dimensional entrainment velocity $u_e$ relative to the tank and (*b*) the difference $u - u_e$. The velocities are made dimensionless using the scale in (6) for the entrainment velocity $u_e$. Negative velocities are towards the plume. Note that the velocity profile for experiment 10 was taken after 90 min had elapsed and is therefore different to those profiles shown in figure 5.

Indeed, in some cases, the velocity at a given depth reversed and fluctuated between two values that were close to local velocity maxima of opposite signs.

The fluctuations in velocity were accompanied by oscillations in the density field. In the absence of internal waves and shear layers, the ‘filling box’ solution predicts that the density increases linearly with time at a fixed point. However, conductivity measurements at a fixed point show that the density oscillated about this linear trend. An example is shown in figure 6, where we plot the density at $\zeta = 0.25$ as a function of time (figure 6*a*) and the deviations from the best-fit linear trend (figure 6*b*) for experiment 10. The period of oscillation $t_o$ (listed in table 1) was measured from the density records for the asymptotic state for each experiment. The periods were all of the order of $(0.3\text{–}0.9)t_a$ and $(50\text{–}200)t_w$.

### 4.3. *Shear layer establishment in existing stratification*

After the tank had been stratified, the plume was turned off and the motions allowed to decay. The plume was later restarted and horizontal velocity profiles were taken at regular intervals. In 12 experiments, the pattern of development of the layers was the same. A sequence of profiles from one run is shown in figure 7. At small times (figure 7*a*), the stratified water above the outflow layer began to move away from the plume and a broad region in the upper half of the box moved towards the plume. Ignoring the effects of stresses imposed by the rigid (no-slip) bottom and the partly-rigid

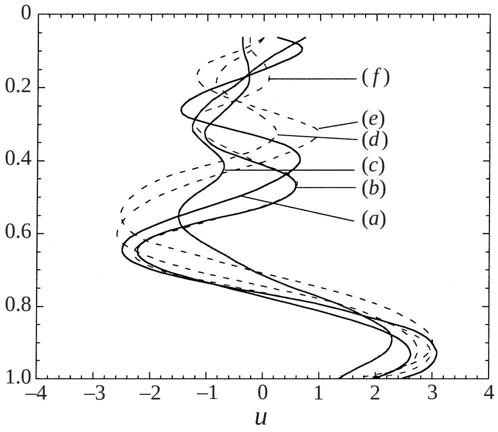

FIGURE 5. Horizontal velocities (made dimensionless using the scale in (6) for the entrainment velocity $u_e$) at 8 min intervals during experiment 10 (see table 1) showing the transition between a five-layered system and a four-layered system and back. (*a*) 62 min, (*b*) 70 min, (*c*) 78 min, (*d*) 86 min, (*e*) 94 min, (*f*) 102 min after start.

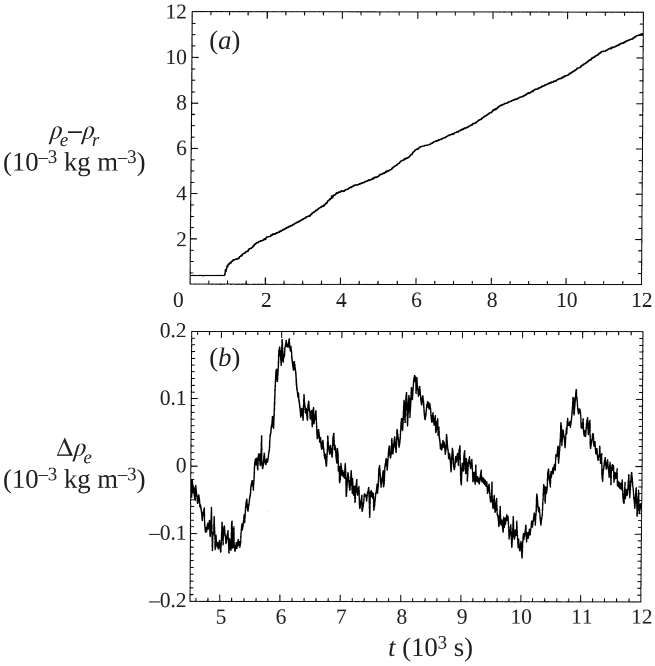

FIGURE 6. The density $\rho_e - \rho_r$ determined from the conductivity probe fixed at 0.175 m from the bottom ($\zeta = 0.25$) in experiment 10. The first front passed the probe at $t = 900$ s. (*a*) The density variation is approximately linear with time long after the first front has passed the probe. (*b*) Deviations $\Delta\rho_e$ from the linear trend in (*a*) show low-frequency periodic oscillations.

(free-slipping) surface at the top, this motion resembled the second baroclinic mode (found in § 5.2 for the ‘filling box’ density profile). The position of the inflow velocity maximum shifted down with time and a third shear layer soon formed at the top (figure 7*b*). We will see below that the motion at this stage appeared to be dominated by the third baroclinic mode. Additional vertical structure continued to develop in the velocity profile, consistent with the appearance of higher baroclinic modes being

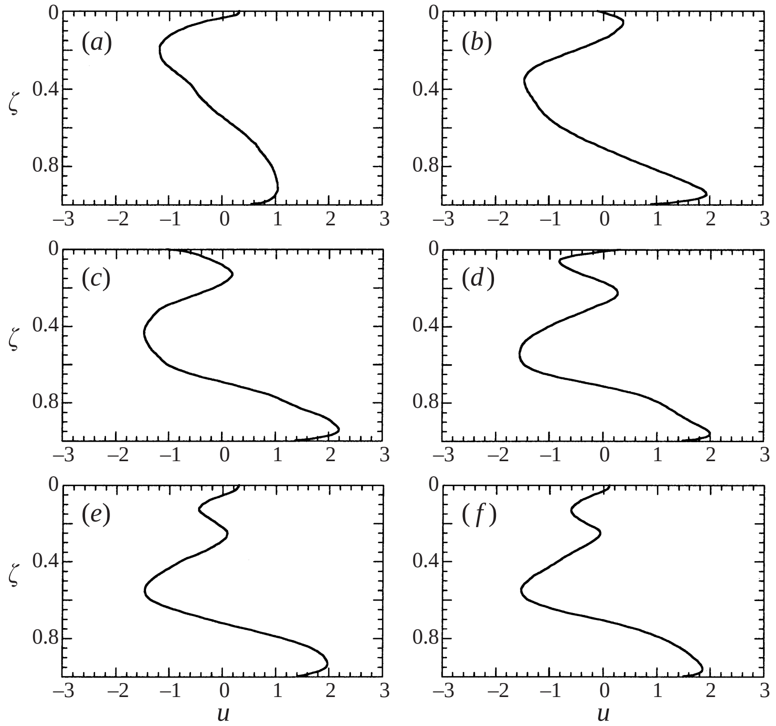

FIGURE 7. The evolution of the baroclinic modes and development of shear layers in a stratified tank initially at rest. These horizontal velocity profiles (made dimensionless using the scale in (6) for the entrainment velocity $u_e$) were taken (*a*) 2 min, (*b*) 4 min, (*c*) 6 min, (*d*) 8 min, (*e*) 10 min, (*f*) 12 min after restarting the plume in experiment 8. The establishment of the velocity structures in all the experiments showed the same behaviour, differing only in the time taken to reach a quasi-steady state.

excited by the bottom outflow, until the velocity profile reached that in figure 7(*f*). The time required for the development of the baroclinic structure was much shorter than the period of the persistent low-frequency oscillations seen in § 4.2. Hence, the structure in figure 7(*f*) was a quasi-steady state. The dominant vertical lengthscale of the velocity profile appeared to be set by the depth of the plume outflow.

We estimated the timescale for establishment of the shear layers by measuring the time $t_e$ taken for the third velocity extremum (from the bottom) to migrate down to the level $\zeta = 0.28$ and for the fourth extremum to reach $\zeta = 0.12$ (the state in figure 7*e*). The plot in figure 8(*a*) of $t_e$ against $t_w$, each normalized by $\overline{N^{-1}}$, shows that the time for the development of the shear layers was proportional to the travel time of internal waves. (Note that both the travel times of internal waves along the length and up through the height of the box are proportional to $\overline{N^{-1}}(L/H)$.) The data are well described by a straight line passing through the origin, $t_e = (12.6 \pm 0.8)\overline{N^{-1}}(L/H)$. Most of the variance in this result, however, can be attributed to the effects of the third independent timescale, $t_a$. A plot of $t_e$ against $t_a$, each normalized by $t_w$, in figure 8(*b*) shows that $t_e/t_w = (15.8 \pm 0.5) - (0.0172 \pm 0.003)t_a/t_w$. Thus, the normalized establishment time was weakly dependent on the advection time, becoming longer for more rapid 'filling box' ventilation. Establishment timescales that are 12 to 15 times the $\overline{N^{-1}}(L/H)$ scale are consistent with the dominance of higher baroclinic modes which have smaller phase speeds. For instance, if the total water depth $H$ in

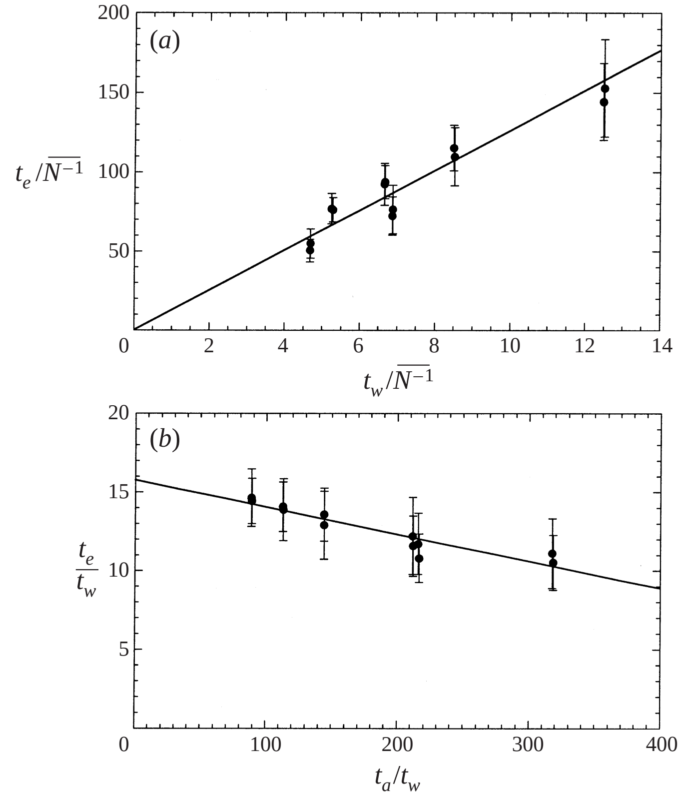

FIGURE 8. Time $t_e$ taken for the velocity structure to evolve to that shown in figure 7(*e*). (*a*) $t_e$ is plotted against $t_w$, the timescale for long internal waves to travel the length of the tank, both non-dimensionalized by $\overline{N^{-1}}$. (*b*) $t_e$ is plotted against $t_a$, the timescale for vertical advection in the 'filling box' model, both non-dimensionalized by $t_w$. Note that in (*a*) the abscissa reduces to $t_w/\overline{N^{-1}} = L/H$.

the wave-speed scale is replaced by $\frac{1}{4}H$, the dominant vertical scale of forcing, then $t_e$ indicates that these higher modes traverse the length of the tank only a few times before the quasi-steady flow is established.

In order to place the rate of vertical advection in perspective, we note that the quasi-steady shear layers were established in a time of the order of one-tenth of the advection timescale, the time required for the tank to be refreshed with new plume water. This is illustrated in figure 9, which shows the distribution of water from the plume at a time approximately $t_e$ after the restart. The dye from the restarted plume had reached only heights below $\zeta = 0.65$ (and the vertical velocity decays rapidly with height (4*a*)), whereas the velocity structure was already approaching the final quasi-steady state.

## 5. Discussion

In this section, we present further detail on the shear layers, beginning in § 5.1 with a summary of the shear layers as seen in the collection of experiments described in § 3. In § 5.2, we calculate the inviscid baroclinic normal modes for the density stratification (4*c*) and show that the vertical scale of the shear layers decreases with

FIGURE 9. The shear-layer structure developed throughout the tank at the time the dyed outflow from a restarted plume in a previously established density gradient had been advected upward to $\zeta = 0.65$.

distance from the bottom. The effect of viscosity on the normal modes is examined using a theoretical analysis in § 5.3 for a linear density stratification. The horizontal velocities in the shear layers are then adjusted in § 5.4 using a heuristic approach to take into account both viscosity and the nonlinear density stratification (4*c*). Finally, in § 5.5, we compare the shear layers with similar well-known flows.

### 5.1. *The circulation pattern*

The large-time circulation pattern in a 'filling box' could be divided broadly into three regions: the bottom outflow layer, the central region of the water column and the near-surface region. The plume outflow was a gravity current which occupied the bottom quarter of the tank ($0.75 < \zeta < 1$). This region was dominated by convection and not greatly influenced by wave motions in the overlying stratified water. Under the conditions of our experiments, it was also a turbulent layer. The dimensionless thickness of the outflow layer did not vary significantly, despite large variations in the dimensions of the tank. Assuming no interference between the plume and the tank walls, the height $H$ of the source is the sole external lengthscale available to influence the plume and its volume flux. Hence, the bottom outflow is expected (and observed) to be a fixed fraction of the source height. If the outflow is homogeneous, we might also expect the dimensionless plume outflow depth to be larger for narrower tanks with both the source height and buoyancy flux held constant. However, this was not the case (see figure 4, where the outflow depth in experiment 2 in a 0.2 m wide tank was actually similar to that recorded for experiment 10 in a 0.3 m wide tank). A possible explanation is that the greater expansion of the outflow in the wider tank led to greater entrainment of overlying water. Another explanation, arising from the conclusions of the analyses in §§ 5.2 and 5.3 below, is that the outflow depth is controlled by the normal mode selected by the system.

The central region of the water column ($0.15 < \zeta < 0.75$) was dominated by baroclinic modes generated by internal gravity waves and was comprised of at least three velocity extrema. The laminar motions in this region were less rapid than the underlying plume outflow from which they apparently derived their energy. The outflow also apparently set the dominant vertical scale corresponding to four to six shear layers through the tank depth. The effects of entrainment into the plume were most noticeable in this central region. The entrainment velocity opposed the flow in the third shear layer from the bottom and reduced its velocity relative to the tank to almost zero. This region also exhibited the greatest low-frequency time-variability in horizontal motion, with periodic reversals in direction and accompanying fluctuations in the density gradient at some depths.

The region very close to the surface ($0 < \zeta < 0.15$) was characterized by a small horizontal velocity towards the plume. The horizontal velocity associated with the baroclinic modes was smaller at these depths than the entrainment velocity $U_e$ into the plume, even though $U_e \rightarrow 0$ at the surface. This region is where both the buoyancy frequency and vertical wavenumber (see below) were largest. The velocity structure close to the surface was also the most variable with time. In the experiments, the flow was sometimes unidirectional and at other times two or three distinct velocity extrema were evident, corresponding to counterflowing shear layers superimposed on the entrainment flow toward the plume.

For a single plume descending in the 'filling box', Baines & Turner (1969) verified the density profile (4*c*) experimentally for the region below the first-front. Agreement between the experimental and theoretical density profiles was achieved even though background motions, now shown to permeate 'filling boxes', do not feature in the model of § 2. Hence, it appears that entrainment into the plume is not affected by the presence of shear layers.

### 5.2. *Baroclinic normal modes*

We assume that (4*c*) defines the stratification in our experiments at large times. In this section, we calculate numerically the first eight baroclinic modes, neglecting the effects of viscosity and the relatively small velocities associated with entrainment and vertical advection. In this and the following sections, $x$ is the distance along the tank, $y$ the height from the bottom, and $u$ and $w$ the usual velocities. The equations of motion in the two-dimensional case are

$$\frac{\partial u}{\partial x} + \frac{\partial w}{\partial y} = 0, \tag{7a}$$

$$\rho_0 \frac{\partial u}{\partial t} + \frac{\partial p'}{\partial x} = 0, \tag{7b}$$

$$\rho_0 \frac{\partial w}{\partial t} + \frac{\partial p'}{\partial y} + \rho' g = 0, \tag{7c}$$

$$\frac{\partial \rho'}{\partial t} + w \frac{d\rho_0}{dy} = 0, \tag{7d}$$

where $\rho'$ and $p'$ are small perturbations of the density and pressure field, respectively. Following Gill (1982), $w$ and $p'$ can be separated into

$$w = \hat{h}(y)\tilde{w}(x,t) \quad \text{and} \quad p' = \hat{p}(y)\tilde{\eta}(x,t).$$

Here, $\hat{h}$ and $\hat{p}$ are the vertical displacement and pressure, respectively, while $\tilde{w}$ has units of inverse time and $\tilde{\eta}$ is dimensionless. With these variables, and using the hydrostatic approximation, equations (7) are separated and reduced to

$$\frac{\mathrm{d}^2\hat{h}}{\mathrm{d}y^2} + \frac{N^2}{c_n^2}\hat{h} = 0, \tag{8a}$$

$$c_n^2 \rho_0 \frac{\mathrm{d}\hat{h}}{\mathrm{d}y} = \hat{p}, \tag{8b}$$

$$\frac{\partial \tilde{w}}{\partial t} - c_n^2 \frac{\partial^2 \eta}{\partial x^2} = 0, \tag{8c}$$

$$\tilde{w} = \frac{\partial \tilde{\eta}}{\partial t}, \tag{8d}$$

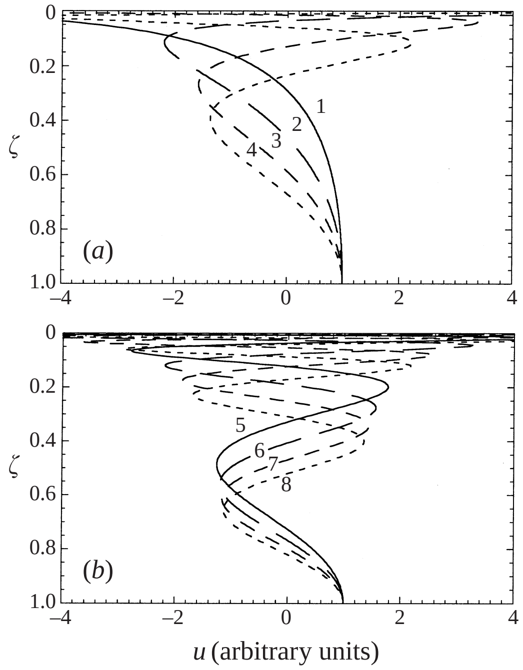

FIGURE 10. Inviscid baroclinic normal modes calculated for the plume stratification (4*c*). (*a*) The first four modes and (*b*) the next four modes. The horizontal velocities have been normalized to give the same value at the bottom.

where $c_n$ is a separation constant. There is an infinite sequence of descending eigenvalues $c_n$, each of which corresponds to an eigenfunction (normal mode) with the relevant boundary conditions being rigid, but free-slipping top and bottom. With a disturbance induced at $y = 0$, the solutions for $\hat{h}$ and $\hat{p}$ are calculated numerically from (8*a*) and (8*b*). Meanwhile, (8*c*) and (8*d*) indicate that $\tilde{\eta}$ satisfies the wave equation. A solution to $\tilde{\eta}$ and $\tilde{w}$ has the form

$$\tilde{\eta} = A\sin(kx + \omega t), \qquad \tilde{w} = A\omega\cos(kx + \omega t), \tag{9}$$

where the frequency is related to the horizontal wavenumber by $\omega^2 = c_n^2 k^2$. Note that $k$ (and hence $\omega$) depends on the horizontal mode of the waves. The horizontal velocity is also separable in the form

$$u = \frac{\hat{p}(y)}{g\rho_0(y)}\tilde{u}(x,t),$$

and can be calculated from the solution to (8). If the frequency is zero (as for columnar baroclinic modes in an infinitely long tank), $\tilde{w}, \tilde{\eta}$ and $\tilde{u}$ do not vary with time, so that for fixed $x$, the horizontal velocity is proportional to $\hat{p}(y)/g\rho_0(y)$. Figure 10 gives the functional dependence of $u$ on the dimensionless depth $\zeta$ for the first eight columnar ($\omega = 0$) modes. It shows that for the $n$th mode there are $n + 1$ shear layers (or velocity extrema) whose thicknesses decrease toward the top of the tank. In the experiments, the region at the top of the stratification is characterized by very large density gradients, and is therefore expected to be significantly altered by diffusion. In addition, the very small vertical scales of motion in this region are expected to be

| Mode $n$ | Eigenvalue $c_n$ (ms$^{-1}$) | Period of horizontal oscillations $T_n$(s) |
|---|---|---|
| 1 | 0.0331 | 66.4 |
| 2 | 0.0203 | 109 |
| 3 | 0.0140 | 157 |
| 4 | 0.0106 | 208 |
| 5 | 0.00843 | 261 |
| 6 | 0.00701 | 314 |
| 7 | 0.00600 | 367 |
| 8 | 0.00525 | 419 |

TABLE 2. The eigenvalues and periods of horizontal oscillations for the normal modes in experiment 10.

removed by viscous effects, and so we will focus on the region $0.05 < \zeta < 1$, where the $n$th mode, for $4 \leqslant n \leqslant 8$, has $n-1$ velocity extrema.

In the experiments, the modes that were excited most strongly at asymptotically large times were those that had vertical lengthscales at the bottom of the tank similar to the plume outflow depth. The measured horizontal velocity profiles (figure 4) in the region $0.1 < \zeta < 1$ are qualitatively similar to the velocity structures of the sixth, seventh and eighth inviscid columnar modes, except that the amplitudes of the horizontal velocities increase with height in the inviscid modes. In particular, the third and fourth horizontal velocity extrema of the $n = 7$ columnar mode lie at $\zeta = 0.35$ and $\zeta = 0.19$, consistent with our experimental observations. This mode also corresponds to six shear layers, as was commonly observed. In contrast, the structures of the lower columnar modes ($n = 1$ to 4) were seen only at short times after the plume was started in the pre-established stratification (§ 4.3). The observations were therefore consistent with the early appearance, particularly in the upper half of the water column, of the most rapidly propagating columnar modes, and with the later appearance of the slower propagating columnar modes, the latter also being the most strongly excited. On the other hand, the measured horizontal velocities decay with height, whereas the calculated columnar modes have amplitudes that increase with height. The difference can be attributed to viscosity which acts most strongly on the smaller vertical scales characteristic of both the higher columnar modes and of the upper more strongly stratified levels of the box. We look more closely at viscous effects in the following sections. Sidewall dissipation in our long channels will further contribute to this decay.

The wave equation constructed from (8*c*) and (8*d*) gives the wave speed $c_n$ for the spectrum of normal modes having horizontal wavenumber $k$. Therefore, we are not restricted to consideration of zero frequency columnar modes. In particular, for a channel of finite length $L$, we assume that the modes of oscillation are the fundamental modes having $u = 0$ at $x = 0$, $L$ and wavenumber $k = \pi/L$. The period $T_n$ of oscillation in each normal mode can then be calculated. Table 2 gives the values of $c_n$ and $T_n$ for each of the first eight normal modes for the conditions of experiment 10. It shows that the modes excited most strongly (the experiments indicate that these are $n = 6$, 7 and 8) are predicted to have periods of approximately 5 to 7 min. Instead, we observed oscillations of very much longer periods, as reported in § 4.2. We note that beating periods between the sixth and seventh modes and between the seventh and eighth modes are approximately 70 and 95 min, respectively. These beating periods are approximately twice the observed period, hence the low-frequency oscillations seen in the experiments are not simply a linear superposition of modes. Oscillations were also observed during both the development and decay of the shear layers (figures 7*a*–7*c*), but are transient in nature and therefore different to the oscillations expected under the large-time normal mode description. In § 5.4, we show that the dominant mode corresponds to a travelling internal gravity wave whose downward phase speed is approximately balanced by the upward vertical advection above the plume outflow. The approximate balance may lead to a quasi-stationary wave field – the observed long-period oscillations at a given height corresponding to a wave mode with much higher intrinsic frequency, but whose phase speed is not exactly balanced by the vertical advection at all heights.

### 5.3. *Analysis for viscous internal waves in a uniform buoyancy frequency environment*

We take as our starting point the two-dimensional linearized equations of motion in (7) with the addition of viscous terms in the momentum equations. Thus, (7*b*) and (7*c*) become

$$\rho_0 \frac{\partial u}{\partial t} + \frac{\partial p'}{\partial x} - \rho_0 \nu \left( \frac{\partial^2}{\partial x^2} + \frac{\partial^2}{\partial y^2} \right) u = 0, \qquad (10a)$$

$$\rho_0 \frac{\partial w}{\partial t} + \frac{\partial p'}{\partial y} + \rho' g - \rho_0 \nu \left( \frac{\partial^2}{\partial x^2} + \frac{\partial^2}{\partial y^2} \right) w = 0. \qquad (10b)$$

The flows in the ‘filling box’ resulting from entrainment and vertical advection have been neglected in the linearized system of equations. Introducing the streamfunction $\psi$ such that $(u, w) = (\partial\psi/\partial y, -\partial\psi/\partial x)$, we can write the system given by (7*a*), (7*d*), (10*a*) and (10*b*) as

$$\left[ \frac{\partial}{\partial t} - \nu \left( \frac{\partial^2}{\partial x^2} + \frac{\partial^2}{\partial y^2} \right) \right] \left[ \frac{\partial}{\partial t} \left( \frac{\partial^2}{\partial x^2} + \frac{\partial^2}{\partial y^2} \right) \right] \psi + N^2 \frac{\partial^2 \psi}{\partial x^2} = 0. \qquad (11)$$

To enable comparison with the scaling approach in § 5.4, we consider the case of a linear density stratification (i.e. $N^2$ = constant) and look for solutions that correspond to a travelling wave in the vertical direction and a standing wave in the horizontal, i.e. $\psi = \bar{\psi} \exp\left[\mathrm{i}(my + \omega t)\right] \sin kx$, where $k$ and $m$ are the respective horizontal and vertical wavenumbers, and $\bar{\psi}$ is a constant. Substituting this form into (11) gives the dispersion relation

$$-\mathrm{i}\nu\omega\kappa^4 + \omega^2\kappa^2 - N^2k^2 = 0, \qquad (12)$$

where the total wavenumber $\kappa^2 = m^2 + k^2$. We again choose the horizontal wavenumber $k = \pi/L$ to correspond to the lowest mode that satisfies the boundary conditions of zero horizontal velocity at $x = 0$, $L$ in the tank. The vertical wavenumber $m$ takes complex values in order to describe the attenuation of the wave motion with height owing to viscosity.

In the present case, shear layers are excited at the base of the tank by the plume outflow. On physical grounds, we consider only internal wave modes that decay with height. This restricts the solution to roots with $\mathrm{Im}(m) > 0$. Moreover, only modes that radiate energy upward from the plume outflow are permissible. For the group velocity to be upward (i.e. downward phase velocity) we require that $\mathrm{Re}(m) > 0$. It can be shown that only one of the four possible roots for $\kappa$ in (12) satisfies these conditions, and that this root corresponds to the dimensionless vertical wavenumber

$$mH=\tfrac{1}{2}\sqrt{\omega' Re}\left[\left(|X|-|\beta|\sin\left(\frac{\phi}{2}\right)+\frac{2\pi^2L'^2}{\omega' Re}\right)^{1/2}+\mathrm{i}\frac{|\beta|\cos(\phi/2)-1}{\left(|X|-|\beta|\sin(\phi/2)+\dfrac{2\pi^2L'^2}{\omega' Re}\right)^{1/2}}\right], \tag{13}$$

where

$$X=\left[\left(|\beta|\cos\left(\frac{\phi}{2}\right)-1\right)^2+\left(|\beta|\sin\left(\frac{\phi}{2}\right)-\frac{2\pi^2L'^2}{\omega' Re}\right)^2\right]^{1/2}, \tag{14}$$

$$\tan\phi=\frac{-4\pi^2L'^2}{\omega'^3Re}, \tag{15}$$

and

$$|\beta|=\left[1+\left(\frac{4\pi^2L'^2}{\omega'^3Re}\right)^2\right]^{1/4}. \tag{16}$$

The dimensionless parameters are the Reynolds number $Re=NH^2/\nu$, the tank aspect ratio $L'=H/L$ and the frequency $\omega'=\omega/N$.

Boundary conditions of zero vertical velocity at the top and bottom of the tank require that the phase of $\psi$ is independent of time. This condition is satisfied only by a trivial solution for $\psi$ and therefore suggests that vertical advection in the ‘filling box’ cannot be neglected with regard to the boundary conditions. We now relax this assumption and introduce a steady and spatially constant vertical velocity field $V_f$ (positive upwards) with which the plume outflow appears to move relative to the fluid, and upon which the wave field is superimposed. Thus, the height $y$ above the plume tank bottom in a laboratory frame of reference is related to the apparent height $y_f$ above the plume outflow in a frame of reference moving with the fluid (as denoted by subscript $f$) according to

$$y=y_f-V_ft, \tag{17}$$

where $t$ is the time elapsed since a fluid parcel left the outflow. The governing equation (11) and the assumed form for $\psi$ applies in the frame of reference moving with the fluid, i.e. $y$ is replaced by $y_f$. In the laboratory frame of reference, using (17), we obtain a stationary wave field,

$$\psi=\bar{\psi}\exp[\mathrm{i}(my_f+\omega t)]\sin kx=\bar{\psi}\exp[\mathrm{i}my]\sin kx, \tag{18}$$

when

$$V_f=-\frac{\omega}{m}, \tag{19}$$

i.e. the tank moves downward with respect to the fluid at a speed that, as we will see later, matches the downward phase speed of the travelling wave modes. Note that $V_f$ is equivalent to upward vertical advection in the ‘filling box’ at speed $V$ relative to the tank. We use the solutions to (11) in the fluid frame of reference by applying the boundary conditions of zero vertical velocity at $y_f=V_ft$ and $y_f=H+V_ft$. We find

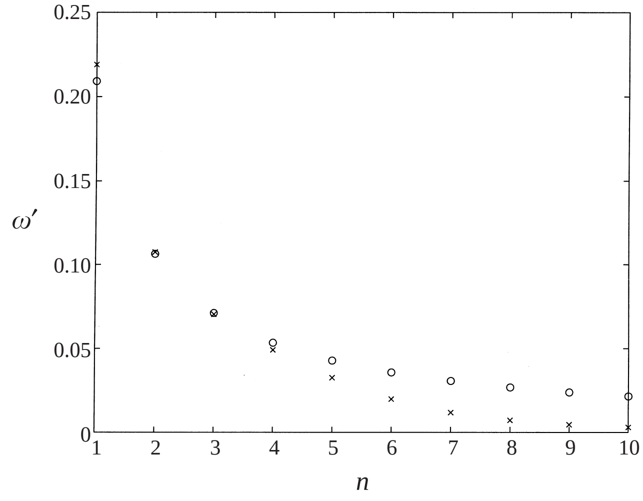

FIGURE 11. The dimensionless frequency spectra as a function of mode number $n$: $x, \omega'_n$ obtained from the analysis for viscous internal waves with parameters appropriate for experiment 10: ($Re = 9000$ and $L' = 0.214$); ○, $\omega'_{i,n}$ obtained for an inviscid fluid.

that $\bar{\psi}$ must be purely real and that, by (13), the vertical wavenumbers satisfy

$$\mathrm{Re}\,(mH) = n\pi = \tfrac{1}{2}(\omega' Re)^{1/2}\left(|X| - |\beta|\sin\left(\frac{\phi}{2}\right) + \frac{2\pi^2 L'^2}{\omega' Re}\right)^{1/2} \quad (n = 1, 2, 3, \ldots). \quad (20)$$

The spectrum of dimensionless frequencies $\omega'_n$ obtained by solving (20) is plotted in figure 11 as a function of $n$ for $Re = 9000$ and $L' = 0.214$. These parameters correspond to experiment 10 if the density gradient in the 'filling box' is approximated by a constant that is equal to the gradient at the tank bottom (i.e. $y = 0$). We discuss the relevance of this approximation later in this section. Also plotted for comparison is the dimensionless frequency spectrum $\omega'_{i,n}$ corresponding to the permissible modes in an inviscid fluid, as given by

$$\omega'_{i,n} = \cos\theta = \frac{kH}{(k^2H^2 + n^2\pi^2)^{1/2}} \quad (n = 1, 2, 3, \ldots) \quad (21)$$

with $kH = \pi L'$. The lowest modes (with least spatial variation) are little affected by viscosity. For $n > 4$, however, the effect of viscosity becomes significant and decreases the frequency of oscillation associated with a particular mode.

The non-dimensionalized attenuation rate associated with the spectrum $\omega'_n$ is given by $\mathrm{Im}\,(mH)$ (from (13)) and is plotted in figure 12 for each $n$, $Re = 9000$ and $L' = 0.214$. For $n > 4$, it can be seen that viscous attenuation over the tank depth ($y/H = 1$) will reduce the modal amplitude by a factor which exceeds $1/e$.

The stationary horizontal velocity structure $u_n(y')$ in the laboratory frame corresponding to each mode $n$ may be calculated as $u = \mathrm{Re}[\partial\psi/\partial y_f]$ and, using (17), written in non-dimensional form as

$$\frac{u_n(y')}{NH} = \frac{|\bar{\psi}|}{NH^2}|mH|\exp\left[-\mathrm{Im}\,(mH)_n y'\right]\cos\left[\mathrm{Re}(mH)_n y' + \Phi\right]\sin(kx), \quad (22)$$

where

$$\Phi = \tan^{-1}\frac{\mathrm{Im}\,(mH)_n}{\mathrm{Re}(mH)_n}, \quad 0 \leqslant \Phi < \frac{\pi}{2}, \quad (23)$$

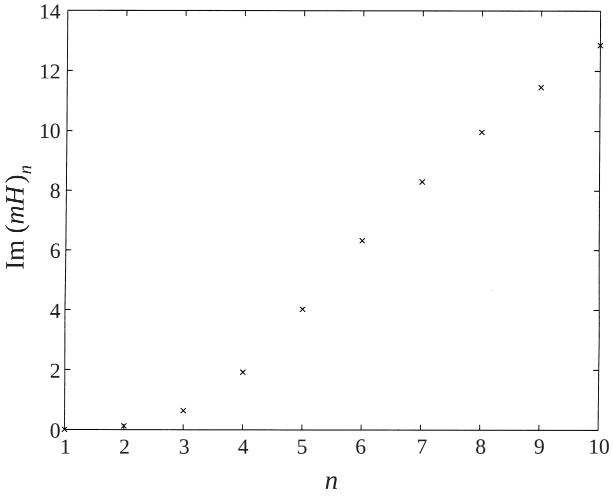

FIGURE 12. The non-dimensional attenuation rate $\mathrm{Im}\,(mH)_n$ corresponding to each mode $n$ predicted by the analysis for viscous internal waves. As in figure 11, the parameters are $Re = 9000$ and $L' = 0.214$.

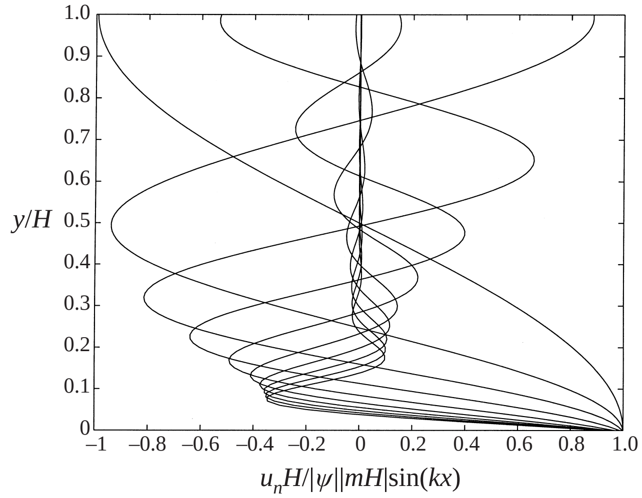

FIGURE 13. The normalized horizontal velocity profile $u_nH/|\bar{\psi}||mH|\sin(kx)$ corresponding to the first 10 modes predicted by the analysis for viscous internal waves. The vertical axis is the non-dimensional height $y/H$ above the tank bottom. As in figures 11 and 12, the parameters are $Re = 9000$ and $L' = 0.214$.

is a constant dependent only upon $mH$. The normalized horizontal velocity profiles $u_n(y')H/|\bar{\psi}||mH|\sin(kx)$ obtained from (22) with $Re = 9000$ and $L' = 0.214$ are given in figure 13. This normalization removes both the variation of $u_n$ with horizontal distance from the plume and the dependence upon the amplitude spectrum $\bar{\psi} = \bar{\psi}(mH)$. Further normalization of the velocity $u_n$ by $|mH|$ ensures that the plotted modes are of a similar amplitude, allowing their structure and attenuation rates to be compared easily. As expected, the higher modes with the most rapid spatial variation are strongly attenuated. It is also evident that the increased attenuation of higher modes means that they are unlikely to have a significant effect on the overall observed flow structure.

The effect of varying the parameters $Re$ and $L'$ on the results in figures 11–13 may be summarized in qualitative terms. An increase in the Reynolds number $Re$ has two effects. The viscous attenuation $\mathrm{Im}\,(mH)$ is reduced and the viscous dispersion relation (20) produces a frequency spectrum approaching that given by the inviscid relation in (21). Decreasing the tank aspect ratio $L'$ while holding $Re$ constant decreases the frequency associated with a given mode, primarily because $kH$ is reduced. To a first approximation, the decrease in frequency is almost linear with $kH$, as can be seen from the inviscid dispersion relation in (21). This decrease in frequency associated with a given mode leads to slower motion and, hence, increased viscous attenuation when $L'$ is decreased ($Re$ held constant).

We have assumed that the quasi-steady flow structure corresponds to a travelling wave mode in the fluid frame whose uniform downward phase speed in the linear stratification is balanced by the uniform upward advection in the tank interior. We now compare the downward phase speed $c_y = \omega/m$ of each wave mode with the vertical advection velocity $V$ for all of the experiments. Two different cases are examined. First, we consider the phase speeds associated with the inviscid baroclinic normal modes of the nonlinear 'filling box' density profile, as found in § 5.2. The dispersion relation for internal waves (e.g. see Lighthill 1978),

$$\omega = N(y)\frac{k}{(k^2 + m^2(y))^{1/2}}, \tag{24}$$

may be used with table 2 to calculate $c_y$ at the level of the plume outflow (i.e. $y = 0$). Secondly, we examine the phase speeds of wave modes in a viscous linearly stratified fluid (uniform $N$), as predicted by the analysis in this section. In the more complex 'filling box' flow, the advection–phase speed balance is again anticipated to hold at the level of the plume outflow, where the wave motions are excited. Therefore, the density gradient at the outflow level (taken to be the tank bottom) determines the properties of waves above this level. Hence, the results from this section may be related to those from § 5.2 by equating the density gradient of the linear stratification with that at the base of the 'filling box' density profile. Equation (20) derived for the linear stratification can then be used to estimate $\omega$, and thus $c_y$ for each wave mode in the nonlinear stratification. Further, the vertical advection in the linear stratification is taken to be equal to that at the base of the 'filling box', i.e. $V(y = 0)$.

We plot $c_y(y = 0) - V(y = 0)$ versus the mode number $n$ in figures 14(*a*) and 14(*b*) for the two respective cases. Figure 14(*a*) suggests that the upward advection in the 'filling box' can be balanced by the downward phase speed of a mode with $n$ greater than 7 (i.e. more than 8 shear layers) over the range of experimental parameters. This compares with 5 or 6 shear layers typically observed in experiments. Figure 14(*b*) illustrates the effect that the linear stratification approximation has on the shear layer structure; the advection–phase speed balance is now achieved by modes with $n$ between 2 and 4 (i.e. between 3 and 5 shear layers). The reason for this difference is that the density gradient and hence the wavenumber both increase with height in the 'filling box' density profile, leading to an increase in the number of shear layers. However, the linear stratification approximation is useful because it provides a simpler means of predicting the dominant wavenumber near the bottom of the tank. This is illustrated in figure 15, where the dimensionless vertical wavenumber $mH$ is plotted as a function of $c_y(y = 0) - V(y = 0)$ for each experiment. The vertical wavenumber of quasi-stationary modes, whose phase speed approximately balances the vertical

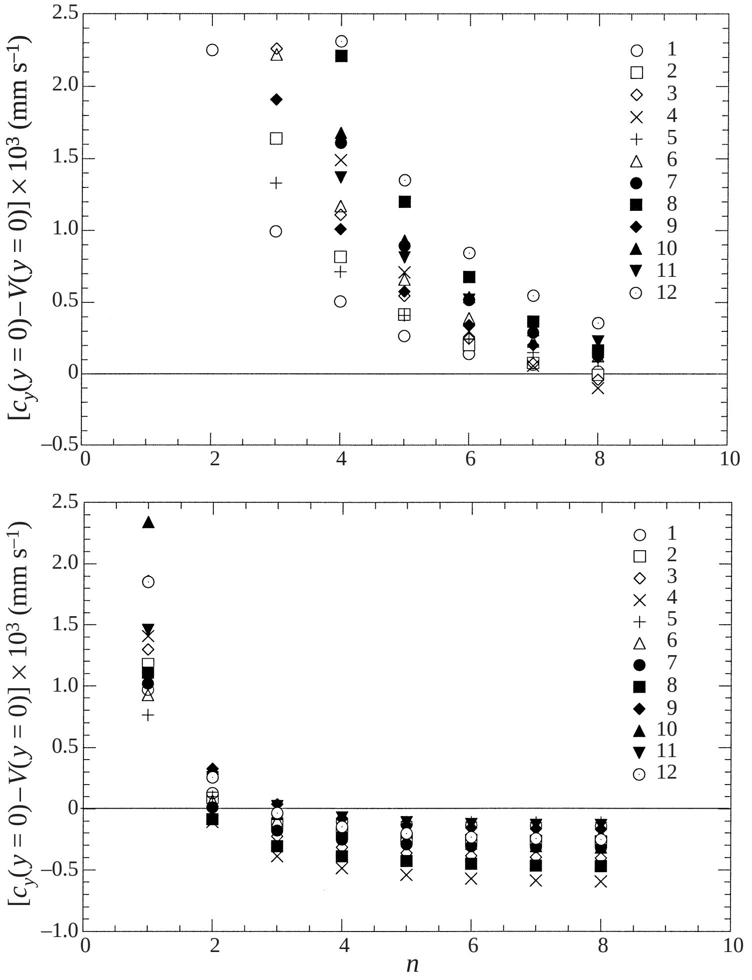

FIGURE 14. Plot of the difference between phase speed and vertical advection speed as a function of the mode number $n$ (points denoted by discrete symbols) in each experiment for (*a*) the inviscid baroclinic modes in a 'filling box' density stratification with no vertical advection, and (*b*) the modes in viscous linearly stratified fluid with uniform vertical advection. Values of $c_y(y=0) - V(y=0) \approx 0$ (where $c_y$ is positive downwards and $V$ is positive upwards) indicate modes that are approximately stationary in the laboratory frame of reference.

advection, is indicated by points for which $c_y(y=0) - V(y=0) \approx 0$. Dimensionless vertical wavenumbers in the range 6–11 are predicted for both the 'filling box' density profile (figure 15*a*) and the linear stratification (figure 15*b*).

The horizontal velocity $u_n$ for each mode $n$ given by (22) first becomes zero at a level

$$\frac{y_n}{H} = \frac{\pi/2 - \Phi_n}{\mathrm{Re}\{mH\}_n} \tag{25}$$

above the tank bottom. The dominant mode predicted for a linear stratification is in the range $n = 2$–$4$ (wavenumber $\mathrm{Re}\{mH\} = 6$–$11$) and, allowing $\Phi$ to vary between the limits in (23), corresponds to a 'shear layer' of depth up to $0.26H$ at the tank bottom. This depth range encompasses the observed plume outflow depth (i.e.

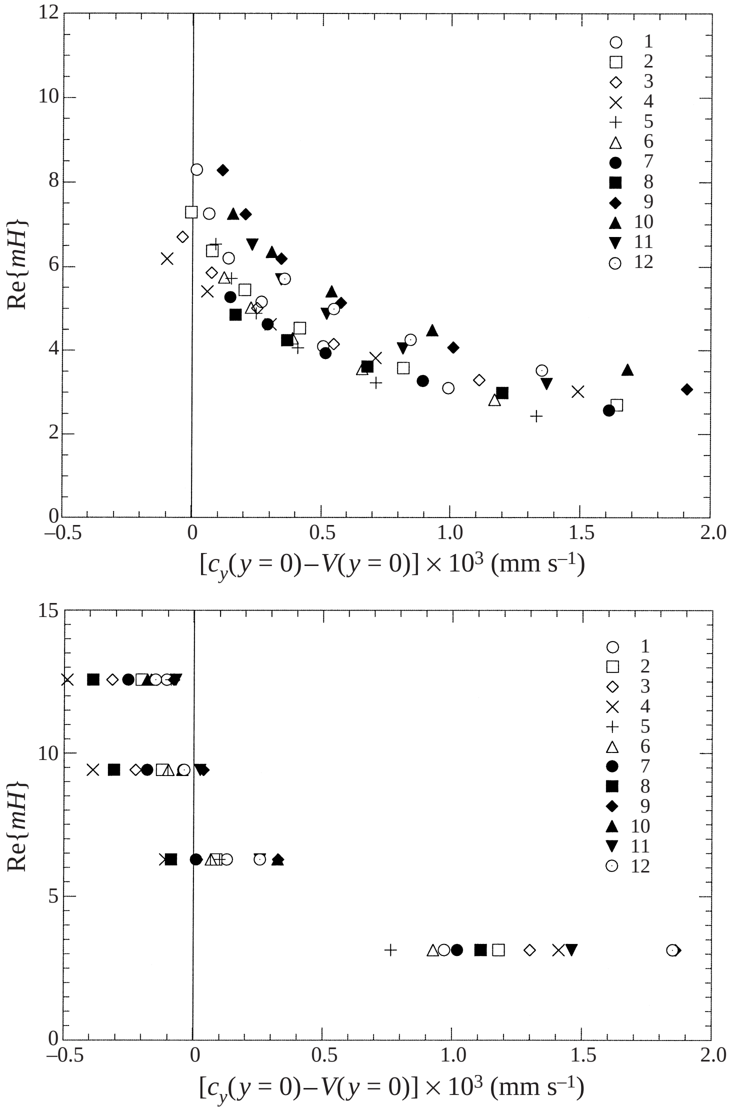

FIGURE 15. Plot of the dimensionless vertical wavenumber $mH$ predicted for each mode (points denoted by discrete symbols) over the range of experiments for (*a*) the inviscid baroclinic modes in a ‘filling box’ density stratification with no vertical advection, and (*b*) the modes in viscous linearly stratified fluid with uniform vertical advection. The dimensionless wavenumber $mH$ is plotted as a function of $c_y(y=0) - V(y=0)$, and values of $c_y(y=0) - V(y=0) \approx 0$ indicate modes that are approximately stationary in the laboratory frame of reference.

approximately $\frac{1}{4}H$), but a more careful approach, which takes account of variations in both the phase constant $\Phi_n$ in (25) and the dominant modes in each experiment, suggests the zero-velocity level corresponds more closely with the outflow depth. Figure 16 is a plot of the variation of the dimensionless zero velocity level $y_n/H$ as a function of $c_y(y=0) - V(y=0)$. The bottom shear layer depth is expected to lie in the approximate range 0.15–0.26$H$ in a linear stratification; the ‘filling box’ flow might be anticipated to decrease these values slightly, as discussed in § 5.4.

Although the plume outflow is turbulent and essentially forced by an external

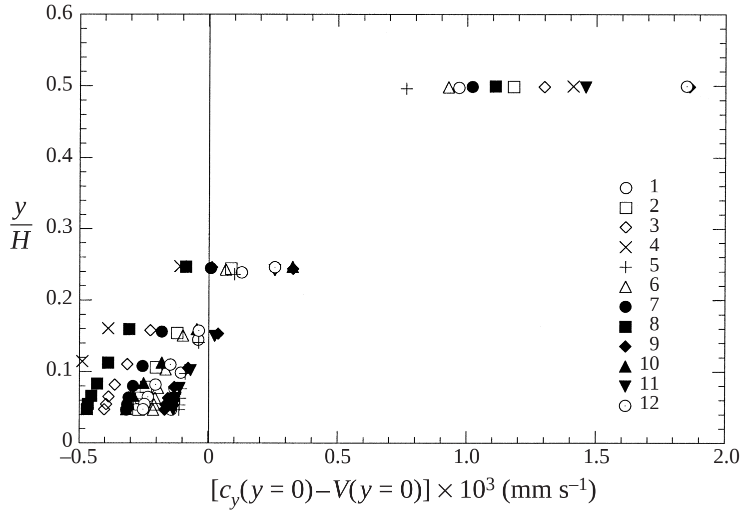

FIGURE 16. The dimensionless zero velocity height $y_n/H$ predicted for each mode (points denoted by discrete symbols) over the range of experiments. The dimensionless height $y_n/H$ is plotted as a function of $c_y(y=0) - V(y=0)$, and modes with $c_y(y=0) - V(y=0) \approx 0$ indicate the expected depth of the bottom shear layer.

process, we expect that the wave field and the outflow will be coupled. We have not attempted to calculate the amplitude spectrum $\bar{\psi}(mH)$ in (22), but anticipate that modes whose half-wavelength is comparable to the outflow depth will be excited preferentially. As the wave field must be stationary in the vicinity of the outflow, the nature of the coupling will be to influence the outflow depth so as to maintain a stationary wave field. We suggest, therefore, that it is not a coincidence that the observed outflow depth is comparable with that predicted for the bottom shear layer.

Very slow oscillations in the flow are observed at a fixed height (i.e. in the laboratory frame), as described in § 4.2. The analysis in this section cannot capture this behaviour since it contradicts our stationarity assumption. However, we suggest that the slow oscillations of the quasi-steady flow structure are due to the transfer of momentum between the wave field and the mean flow. This interaction is currently the subject of further work.

There are two important conclusions from this section. First, viscosity plays a significant role in attenuating with height the motion in the shear layers. The least rapidly varying wave modes (small $n$) are weakly attenuated and therefore well approximated by the inviscid dispersion relation (21). Viscous attenuation renders more rapidly varying modes unimportant for the flow structure. Secondly, it is apparent that vertical advection in the 'filling box' circulation is crucial in setting the vertical scale of the shear layers.

### 5.4. *Effects of viscosity on horizontal velocities*

It was not possible to include readily in the models of either § 5.2 or § 5.3 the effects of vertical advection in the 'filling box'. Instead, we develop a simpler heuristic model in this section that takes account of the effects of vertical advection, viscous attenuation and the nonlinear density profile in determining the shear layer structure. As in § 5.2, we disregard the horizontal flow due to entrainment of water into the plume.

We assume that a disturbance at the bottom of the tank supplies the energy required to develop and sustain the baroclinic normal modes, but the upward energy and momentum fluxes in internal waves are attenuated by viscosity. In our experiments, the diffusion of momentum acts to reduce velocities in the shear layers, as does viscous dissipation in the boundary layers along the tank walls. However, dissipation in the tank wall boundary layers is neglected here; the conditions under which this approximation is valid are given in the Appendix.

We review some relevant results from the theory of internal wave propagation in a moving stratified fluid (see for example Lighthill 1978). The frequency $\omega$ measured at a fixed point is dependent upon both the rate at which waves are advected past that point and the frequency $\omega_r$ that would be measured locally in a fluid at rest. For mild rates of viscous attenuation, it was shown in § 5.3 that $\omega_r$ will approximately satisfy the inviscid dispersion relation (24), where $N(y)$ is the local buoyancy frequency. For internal waves whose wavelength is much shorter than the scale over which $N(y)$ changes significantly, the frequency $\omega$ remains unchanged along a ray, i.e.

$$\omega = -\omega_r + mV = \text{constant}, \tag{26}$$

where $V$ is the velocity of the fluid. Note that we are dealing with a travelling wave whose phase velocity direction is opposite to the advection velocity, and that the signs in (26) have been chosen accordingly. The observed oscillation period is much longer than values of either $\omega_r$ or $mV$ alone would suggest. Therefore, to a good approximation, we may set $\omega = 0$ in (26). As expected, this approximation gives a stationary wave whose downward phase velocity $c_y = \omega_r/m$ balances vertical advection exactly at all heights. Because horizontal scales are much larger than vertical scales ($k \ll m(y)$), it follows from (24) and (26) that

$$\frac{m(y)}{m(0)} \approx \left[\frac{N(y)V(0)}{N(0)V(y)}\right]^{1/2}. \tag{27}$$

From the inviscid solution in § 5.2, it is already clear that the vertical scale of the shear layers decreases with height because of increasing buoyancy frequency $N(y)$. Equation (27) shows that the vertical scale of the shear layers also decreases as a result of the decrease in vertical advection with height. If we let $h(y)$ represent a vertical scale equivalent to half the vertical wavelength of the mode under consideration, then $h(y) = \pi/m(y)$ is approximately the thickness of the shear layer (i.e. the distance between zero crossings in the vertical profile of horizontal velocity) at $y$. However, $h(y)$ decreases monotonically with $y$, and will not, in general, represent the exact thickness of the shear layer at a given height. Later, we will calculate the value of $m(0)$ from (26); this will determine the thickness of the bottom layer and indicate the dominant mode that we are interested in.

The speed at which energy propagates vertically is $c_{gy}(y) + V(y)$, where

$$c_{gy}(y) = \frac{\partial \omega_r}{\partial m} = \frac{N(y)m(y)k(y)}{|\boldsymbol{k}(y)|^3} \tag{28}$$

is the group velocity relative to the mean vertical flow and $\boldsymbol{k}(y)$ is the wavenumber vector $(k(y), m(y))$. Here, only the fundamental horizontal mode satisfying the boundary conditions at the endwalls is assumed to be important, i.e. the horizontal wavenumber $k(y) = \pi/L$. For $k \ll m(y)$, we have from (24) that $\omega_r \approx N(y)k/m(y)$ and, by (26) and (28), that

$$c_{gy}(y) \approx \frac{N(y)k}{m^2(y)} \approx \frac{\omega_r(y)}{m(y)} = -c_y(y) = V(y). \tag{29}$$

The experiments indicate that motion in the shear layers decays with height. We assume that the variation of horizontal velocity with height may be described by an attenuated sinusoid,

$$\frac{u(y)}{u(0)} = C(y)\cos\left[m(y)y\right], \tag{30}$$

where $C(y)$ and $m(y)$ vary slowly in $y$ relative to $u(y)$. In normalizing $u(y)$ by $u(0)$ we assume any variation of the horizontal velocity with $x$ is removed. Note that the vertical dependence assumed in (30) satisfies the rigid free-slip boundary conditions in the tank. Equation (27) gives $m(y)$; to find $C(y)$ we note that the instantaneous rate of working by viscous forces (Batchelor 1967, p. 152) is

$$\begin{aligned}\theta &= \rho_0 \nu \frac{\partial u_i}{\partial x_j}\left(\frac{\partial u_i}{\partial x_j} + \frac{\partial u_j}{\partial x_i}\right) \\ &\approx \rho_0 \nu \left(\frac{\partial u}{\partial y}\right)^2, \end{aligned} \tag{31}$$

where $\nu$ is the kinematic viscosity. The energy balance in the tank may then be written as

$$\frac{\partial}{\partial y}\left[c_{gy}K\right] = -\bar{\theta} = -\rho_0 \nu \overline{\left(\frac{\partial u}{\partial y}\right)^2}, \tag{32}$$

where $K$ is the energy per unit volume associated with a wavepacket that propagates vertically with the group velocity $c_{gy}$ relative to the mean vertical flow. The overbar represents an average over a wavelength. Note that in an inviscid flow, (32) requires the flux of energy relative to the mean flow to be non-divergent. For the internal wave modes in these experiments, $u(y) \gg w(y)$ and therefore the energy $K(y) \approx \frac{1}{2}\rho_0 u^2(0) C^2(y)$. We introduce a long lengthscale $y'$ over which $K(y'), C(y')$ and $c_{gy}(y')$ evolve and a short lengthscale $y$ over which only $u(y)$ varies significantly. Substituting (29) and (30) into (32) and using (27) gives

$$\frac{\partial}{\partial y'}\left[C^2(y')V(y')\right] \approx -\nu k \frac{N(y')C^2(y')}{V(y')}. \tag{33}$$

Dropping primes, the solution for $C(y)$ is then

$$C(y) \approx \left[\frac{V(0)}{V(y)}\right]^{1/2} \exp\left[-\tfrac{1}{2}\nu k \int \frac{N(y)}{V^2(y)}\,\mathrm{d}y\right]. \tag{34}$$

Returning to the traditional ‘filling box’ solution of § 2, the definition of $y$ gives $\zeta = (H - y)/H$ so that the power series expansion (to three terms) for $N(y)$ obtained from (3) and (4$c$) is

$$\begin{aligned} N(y) &= \frac{F^{1/3}}{2^{2/3}E^{2/3}\pi^{1/3}H^{4/3}}\{2.18\zeta^{-5/3} + 0.279\zeta^{-2/3} + 0.0831\zeta^{1/3} + \cdots\}^{1/2} \\ &= \frac{F^{1/3}}{2^{2/3}E^{2/3}\pi^{1/3}H^{4/3}} n(\zeta), \end{aligned} \tag{35}$$

where

$$n(\zeta) = 1.48\zeta^{-5/6} + 0.0945\zeta^{1/6} + 0.0251\zeta^{7/6} + \cdots. \tag{36}$$

From (3) and (4$a$) the power series expansion (to three terms) for $V(y)$ is

$$V(y) = -\frac{\pi^{2/3}2^{4/3}E^{4/3}H^{5/3}F^{1/3}}{A} f(\zeta), \tag{37}$$

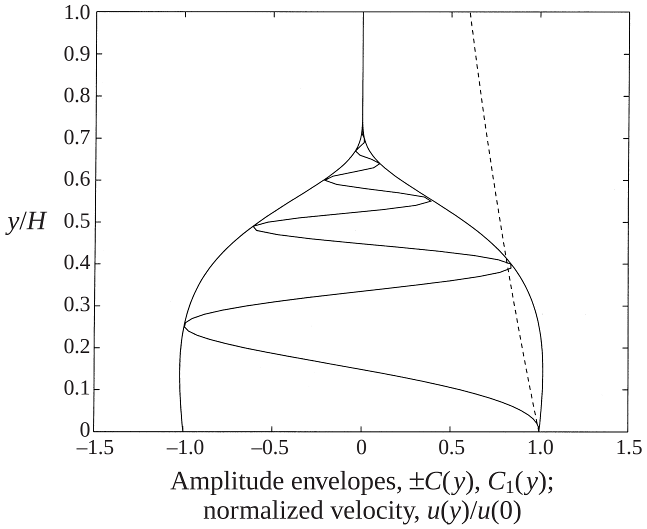

FIGURE 17. Plot showing the amplitude envelope $\pm C(y)$ from (41) together with the normalized horizontal velocity $u(y)/u(0)$ predicted by (27), (30) and (42) for the parameters of experiment 10. - - -, for comparison, the amplitude attenuation function $C_1(y)$ from (43) for the parameters of experiment 10.

with

$$f(\zeta) = 0.460\zeta^{5/3} - 0.0588\zeta^{8/3} - 0.0100\zeta^{11/3}, \tag{38}$$

so that

$$\int_0^y \frac{N(y)}{V^2(y)}\,\mathrm{d}y = \frac{A^2}{\pi^{5/3}2^{10/3}E^{10/3}H^{11/3}F^{1/3}}g(\zeta), \tag{39}$$

where

$$g(\zeta) = -4.00 + 2.21\zeta^{-19/6} + 1.03\zeta^{-13/6} + 0.754\zeta^{-7/6} + \cdots. \tag{40}$$

The solution (34) for the amplitude $C(y)$ can therefore be expressed as

$$C(y) \approx \left[\frac{V(0)}{V(y)}\right]^{1/2} \exp\left\{-\frac{\nu}{2L}\frac{A^2}{\pi^{2/3}2^{10/3}E^{10/3}H^{11/3}F^{1/3}}g(\zeta)\right\}. \tag{41}$$

Equation (41) gives the envelope for the shear-layer amplitude as a function of height, and is plotted in figure 17 for the parameters of experiment 10. Two points are worth noting. First, the amplitude is predicted to increase slightly before decaying with height. At small $y$, the flux of energy $c_{gy}K$ relative to the mean vertical advection is reduced only slightly by diffusion of momentum. However, the group velocity $c_{gy}$ decreases with height and leads to a net increase in the wave energy $K$ per unit volume at small $y$. The effects of viscosity are more noticeable at greater heights where $m(y)$ has increased significantly. The horizontal velocities observed in experiment 10 (figure 5) perhaps lend qualitative support to this behaviour. Rather than clearly decreasing with height, the two lowest shear layers are approximately equal in magnitude.

Secondly, the envelope (41) will decay more rapidly with height when the initial wavenumber is larger. This dependence is incorporated implicitly in (41) as a consequence of assuming the wave field to be stationary in deriving (27). From (29), the vertical wavenumber at the tank bottom is

$$m(0)H = \left(\frac{N(0)H}{V(0)}kH\right)^{1/2} = \left[\frac{B^{1/2}}{2EH^{1/2}}\right]\left[\frac{n(\zeta=1)}{f(\zeta=1)}\right]^{1/2} = 2.02\left[\frac{B^{1/2}}{2EH^{1/2}}\right], \tag{42}$$

and the predicted values of $m(0)H$ for each experiment are listed in the last column of table 1. Note that these values are comparable to those expected from the curves corresponding to each experiment in figure 15. Using (42), we can express (41) as

$$C(y) = \left[\frac{f(\zeta=1)}{f(\zeta)}\right]^{1/2} \exp\left[-\frac{m^4(0)H^4}{2\pi ReL'}\frac{f^2(\zeta=1)}{n(\zeta=1)}g(\zeta)\right], \tag{43}$$

where the Reynolds number $Re = N(y=0)H^2/\nu$, and the tank aspect ratio $L' = H/L$.

The velocity profile $u(y)/u(0)$ is plotted in figure 17 for the parameters of experiment 10 using (27) and (42). The main features of the observed profiles in figure 5 are reproduced. The velocity profile decays significantly within the depth of the tank and has approximately six shear layers, broadly consistent with the experiments.

We now discuss the discrepancies in the solution. First, almost no motion is predicted above the height $y = 0.7H$, whereas weak shear layers are observed in this region. Secondly, the predicted variation of velocity with height is more rapid than observed. The reasons for these discrepancies are in part related. We predict too large a wavenumber at the tank bottom, which leads to more rapid attenuation of the motion with height owing to increased velocity gradients in shear layers of smaller thickness. Equation (43) reveals just how sensitive the predicted attenuation rate will be: it depends on the fourth power of the wavenumber $m(0)H$. Our prediction of the vertical wavenumber is based on the buoyancy frequency and vertical advection given by the ‘filling box’ theory at the tank bottom, where the wave field is excited. However, the plume outflow is turbulent and the resultant mixing will tend to reduce the local density gradient; indeed the ‘filling box’ solution is valid only at depths of inflow to the plume. This reduction in $N(0)$ will, by (42), lead to a less rapid variation of velocity with height and hence less attenuation than predicted by (34).

A reduction of the local buoyancy frequency $N(0)$ by the turbulent outflow will also increase the depth of the ‘shear layer’ at the tank bottom. The plot in figure 17 for experiment 10 predicts the bottom shear-layer depth to the approximately $0.15H$. In § 5.3, we predicted the dominant internal wave mode to be approximately $n = 3$ in experiment 10 with the depth of the shear layer at the tank bottom being approximately $0.18H$ (see figure 16). This estimate corresponds to the expected height of zero velocity of $0.18H$ based on a constant wavenumber of $m(0)H = 8.8$ (see table 1) for experiment 10. Note that the analysis in § 5.3 was for a linear stratification with uniform advection, and that we would expect this depth to be reduced in a ‘filling box’ owing to the increase in wavenumber with height. However, observations for experiment 10 in figure 5 suggest that the outflow depth was closer to $0.25H$.

A further reason why the flow in the upper part of the tank is not correctly modelled is that the assumption of a scale separation between $y'$ and $y$, used to obtain (33), becomes invalid. Indeed the theory predicts its own downfall, as can be seen in figure 17 above $y \approx 0.5H$, where $C(y)$ has an e-folding scale comparable with the wavelength. Thus, the velocity profile (30) cannot be substituted into (32) while neglecting the variation with $y$ of the amplitude and wavenumber in the upper part of the tank. If this assumption is relaxed, a nonlinear equation for $C(y)$ is obtained in place of (33). Although this equation cannot be solved readily in an analytical form, it is apparent that the effect of the nonlinear terms will be to reduce the rate of attenuation with $y$ of the amplitude function $C(y)$.

In order to show the significance of an increasing wavenumber with height as given by (27), and to allow comparison with the theoretical model in § 5.3, we also give an alternative solution $C_1(y)$ to (33) for uniform vertical wavenumber by assuming $N(y) = N(0)$ (i.e. a linear density gradient) and $V(y) = V(0)$:

$$C_1(y) = \exp\left\{-\frac{\nu}{2L}\frac{A^2}{\pi^{2/3}2^{10/3}E^{10/3}H^{11/3}F^{1/3}}\frac{n(\zeta=1)}{f^2(\zeta=1)}\frac{y}{H}\right\}$$
$$= \exp\left[-\frac{m^4(0)H^4}{2\pi ReL'}\frac{y}{H}\right]. \tag{44}$$

Thus, $C_1(y)$ has the same dependence on the experimental parameters as does $C(y)$. Hence, smaller tank aspect ratios and weaker buoyancy fluxes (resulting in weaker stratification and reduced Reynolds number) should result in greater attenuation of motion with height. These conclusions are in agreement with the qualitative observations in § 5.3, where decreasing either the Reynolds number or the tank aspect ratio increased the attenuation. The attenuation rate given by (44) is plotted in figure 17 for the parameters of experiment 10. Comparison of $C_1(y)$ with the amplitude variation of the $n = 3$ mode in figure 16 (predicted in § 5.3 as most likely to dominate in experiment 10) shows that (44) is a good approximation to the more rigorously derived result. In the lower part of the tank ($y < 0.4$), where variations in $N(y)$ and $V(y)$ are relatively small, the two functions $C(y)$ and $C_1(y)$ behave in a similar manner. However, above this level, $C(y)$ decreases very much more rapidly than $C_1(y)$, indicating that the attenuation rate is highly sensitive to the decreasing vertical scale of the shear layers.

In our experiments, the parameter $m^4(0)H^4/2\pi ReL'$ in (42) and (44) lies in the range 0.07–0.64 with the exception of four experiments (1, 5, 9 and 11), where it is larger (1.67–2.63). These four larger values correspond to a subset of the experiments in which the horizontal velocities were noted to decay especially quickly with height, thus providing some confirmation of our parameterization.

An additional check of the heuristic theory in this section can be made by comparing the observed plume outflow velocity with a prediction based on the plume volume flux and the velocity profile in (30). We assume that the downward volume flux in the plume at the top of the outflow is approximately $\pi R^2 W(\zeta = 0.75)$, and that this volume flux is equal to that in the outflow. Upon integrating (30) across the bottom shear layer, and using (3), (4*a*) and (6), we predict the dimensionless outflow velocity to be

$$u(0) \approx 0.254\frac{L}{L-x}m(0)H. \tag{45}$$

Here, we have assumed that neither $C(y)$ nor $m(y)$ vary significantly in (30) across the shear layer (see figure 17) and are, therefore, approximated well by the values $C(0)$ and $m(0)$, respectively. The velocity profiles in figures 4, 5 and 7 were measured at $x = \frac{1}{2}L$ and for experiment 10 we predict $u(0) \approx 0.5m(0)H = 4.4$, which is similar to the observed values in the range 2–3. However, it is not surprising that (45) overpredicts the observed values. First, (42) overestimates $m(0)H$, requiring the plume volume flux to be carried in a shallower and faster bottom shear layer. Secondly, our estimate in (45) takes no account of the tank geometry. The presence of three tank walls adjacent to the axisymmetric plume might be expected to reduce the velocity in the approximately two-dimensional outflow.

In summary, the predicted horizontal velocity profile (e.g. figure 17) provides strong evidence that the shear layers are the result of baroclinic normal modes subject to the effects of viscosity. Diffusion of momentum owing to viscosity causes the maximal horizontal velocity in successive shear layers to decrease with height so that horizontal motions near the top of the water column have decayed essentially to zero. Although the calculated horizontal velocity profiles do not give shear layers whose vertical extent or individual thickness correspond precisely to observations, we have demonstrated that these details are very sensitive to the wavenumber $m(0)H$ at the tank bottom. Hence, a small error in estimating $m(0)H$ could conceivably account for the discrepancies between predictions and observations.

The effects on internal wave modes of plume entrainment in the environment have not been quantitatively explored. At shallow depths, where the magnitude of horizontal velocities attributed to normal modes are smaller than or comparable to the entrainment velocity towards the plume, fewer layers will be apparent. This effect is likely to involve nonlinear interactions, and may be a factor in the discrepancy between the calculated horizontal velocities of figure 17 and the observations from experiment 10 in figure 4(*a*).

### 5.5. *Comparisons with other shear flows*

The horizontal shear layers found in the plume experiments show similarities to the circulation observed in several other systems. Imberger, Thompson & Fandry (1976) studied experimentally and numerically the two-dimensional flow resulting from the withdrawal and intrusion of fluid from mid-depth in a uniformly stratified tank. They studied a variety of cases based on a parameter $R = Q(NL^2/\nu)^{2/3}/NL^2$, which is the product of the Froude number and one-third power of the Grashof number ($Q$ is the volume flux per unit width). For the case where $R > 1$ (supercritical flow dominated by buoyancy and inertia, with relatively unimportant viscous effects), they showed that convection was the dominant force behind the flow and that internal waves propagated vertically until the induced flow was equal and opposite to the wave phase velocity. The thickness of their withdrawal/intrusive layer was found to be of $O(Q^{1/2}/N^{1/2})$, which is consistent with the lengthscale predicted in (42). Manins (1976) studied intrusions into a linearly stratified fluid for $100 < Re^* < 500$ (where $Re^*$ is the Reynolds number based on the intrusion. Note that this is a different definition to that used in § 5.3). The intrusions were governed by an inertia–buoyancy balance and forced a shear-layer type flow to develop. Above and below the intrusion a series of equal thickness layers formed, between which the horizontal velocity alternated in direction. Dimensional arguments predicted the intrusion thickness again to be of $O(Q^{1/2}/N^{1/2})$; the average intrusion half-thickness measured in experiments was $0.15H$ and compares favourably with our predictions in § 5.4. In the present experiments, we evaluate $R \sim 10$ (based on the volume flux at the base of the plume and the buoyancy frequency $(\overline{N^{-1}})^{-1}$ and $Re^* \sim 400$ (based on the velocity and depth of the plume outflow layer). Hence, these parameters confirm that our ‘filling box’ flows are dominated near the tank bottom by inertia and buoyancy and are in the same regime as the previous studies of intrusions. However, the value of $Re^*$ is sufficiently small that viscosity is important in the upper levels of the tank where $N$ is much greater.

Stratified flows with very small Froude numbers give qualitatively similar behaviour. For example, Martin & Long (1968) studied the equations describing the generation of columnar modes or ‘upstream wakes’ due to a thin, flat plate moving slowly in the horizontal through a uniformly stratified fluid. Viscosity played an important part in this flow and the disturbance produced an alternating layer structure with amplitudes decreasing away from the plate, similar to the flow in our experiments. In a related problem, Bretherton (1967) studied the flow generated by a cylinder moving slowly in the horizontal through a stratified fluid. At large distances ahead of the cylinder, the uniform velocity profile was first perturbed by the arrival of rapidly propagating long wavelength internal gravity waves. Some time later, the arrival of slower waves of short vertical wavelength produced a 'plug flow' confined approximately to the horizontal projection of the obstacle, and with velocity reversals above and below. The equivalent Froude number for our experiments is $16QN^{-1}/H^2 \sim 0.6$ (based on the outflow height $\frac{1}{4}H$). Thus, our conclusion in § 5.4, that viscosity is a strong controlling influence in the upper levels of the water column as a consequence of the increased buoyancy frequency, is consistent with the previous studies of viscous upstream columnar wakes.

## 6. Conclusions

The stratified environment produced by a turbulent plume supports a series of shear layers superimposed on the steady vertical advection and horizontal entrainment flows driven by the plume. These layers are the result of a continuous excitation by the dense plume outflow of baroclinic wave modes whose downward phase speed approximately balances the upward advection in the 'filling box' in the vicinity of the outflow. This approximate phase speed–advection balance also holds throughout the 'filling box', leading to a shear-layer structure that is quasi-steady in the laboratory frame. The dominant wave mode is found to have a vertical scale near the tank bottom that is comparable with the observed turbulent outflow from the dense plume. We suggest that the outflow is not independent of the wave field, and, therefore, that the dominant baroclinic mode is responsible for setting the outflow depth. The baroclinic modes are established on the timescale for the propagation of internal waves through the box and develop rapidly compared to either the ventilation of the box by vertical advection or the rate of change of the 'filling box' stratification in its transient stages. Under laboratory conditions, the gravity current outflow from the base of the plume is characterized by a moderate-to-low Froude number.

Experiments and analysis suggest that viscosity becomes a controlling influence on the upward momentum flux and causes the amplitude of horizontal velocities in the shear layers to decrease with increasing height from the base. Owing to both the large increase in buoyancy frequency and the decrease in vertical advection towards the top of the 'filling box', the shear layer depths decrease with height. At large times, when the stratification has achieved its constant shape, the baroclinic modes also undergo a very low-frequency oscillation between the five-layer and six-layer states (dominated by modes $n = 6$ and 7, respectively). We suggest that this oscillation is due to the transfer of momentum between the wave field and the mean flow. This interaction is currently the subject of further work.

The presence of the shear layers is an interesting aspect of the 'filling box' convection. Although they have little effect on the stratification in that the density surfaces are tilted only slightly in connection with the horizontal motion, the perturbed circulation pattern will have large implications for the transport of both individual water parcels and tracers in the system. For example, tracers released from a source at a fixed depth in the water column, or from a mid-depth outflow produced by a second plume with a smaller buoyancy flux, will spread laterally under control of the interior flows driven by the strong plume. This observation is likely to be relevant to small bodies of water such as lakes and fiords, and is possibly relevant to the oceanic thermohaline circulation. For example, consider an idealized 1 km × 10 km rectangular lake in which a stratification ($N = O(10^{-2})\,\mathrm{s}^{-1}$ and depth of $O(100)$ m) is maintained by a melt-water input. Shear layers with thickness of $O(10)$ m would be expected to form on the timescale of a day. Attenuation of the motion with height increases with the parameter $m^4(0)H^4/2\pi ReL'$, which in our experiments was in the range $O(10^{-1})$–$O(1)$. Similar observations would be expected in our example lake, where this attenuation parameter takes a value between $O(10^{-1})$ and $O(10)$ depending on whether a laminar ($\nu = 10^{-6}\,\mathrm{m^2\,s^{-1}}$) or turbulent 'viscosity' (e.g. $\nu_t$ up to $10^{-4}\,\mathrm{m^2\,s^{-1}}$) is used to characterize the diffusion of momentum. In the oceans, there are a number of sources of intermediate and deep water, each involving vertical convection and outflows that contribute to the water properties, the density stratification and the forcing of the deep circulation. In addition, the characteristic vertical profile of buoyancy frequency in mid-latitude oceans is not dissimilar to that generated by plumes in the 'filling box' model. Thus, the sources having the greatest buoyancy fluxes may conceivably produce baroclinic shear layers qualitatively similar to those observed in our experiments while contributing to the maintenance of the oceanic stratification. However, the downward volume flux of deep water is balanced by a relatively slow upwelling over the vast area of the ocean basins. Therefore, the dominant wave modes corresponding to shear layers are expected to be characterized by a small downward phase velocity, small wavelength and hence large attenuation (values of the parameter $m^4(0)H^4/2\pi ReL'$ of $O(10^2)$–$O(10^4)$ are estimated). The effect of the Earth's rotation may, however, play an important role in confining stronger shear layers to a small portion of an ocean basin, and this is the subject of further investigation.

We are grateful to J. W. Rottman for the use of his computer program to calculate the inviscid baroclinic normal modes. We thank T. Beasley, D. Corrigan and R. Wylde-Browne for their assistance with the experiments and photography. We also thank R. C. Kerr, J. S. Turner and two anonymous referees for their helpful comments on earlier drafts. The receipt of an Australian Postgraduate Award and John Conrad Jaeger Scholarship by A. B. D. W. is gratefully acknowledged.

## Appendix. Neglect of sidewall boundary layers

We have neglected in this paper the flux of horizontal momentum due to viscosity into the sidewall boundary layers. We now justify this assumption.

The ratio $R$ of horizontal to vertical flux of horizontal momentum is

$$R = \frac{\nu \partial^2 u/\partial x^2}{\nu \partial^2 u/\partial y^2}. \tag{46}$$

If the sidewall boundary-layer thickness is of $O(\delta)$ and the shear-layer depth is of $O(m^{-1})$, the volume-averaged ratio of horizontal to vertical flux of momentum is

$$\bar{R} \sim O\left(\frac{1}{m^2 \delta B}\right), \tag{47}$$

where $\bar{R}$ denotes averaging of $R$ from (46) over a shear layer. We may estimate the sidewall boundary-layer thickness as

$$\delta \sim (\nu T)^{1/2}, \tag{48}$$

where $T$ is the timescale over which the boundary layer develops. This timescale is determined by the background vertical advection $V(y)$ in the tank, i.e. $T \sim O(m^{-1}V^{-1})$. Thus, (47) becomes

$$\bar{R}(y) \sim O\left(\left[\frac{V(y)}{\nu B^2 m^3(y)}\right]^{1/2}\right). \tag{49}$$

The relative dissipation in the sidewall boundary layers is greatest at $y = 0$, where the vertical advection $V(y)$ and the vertical wavenumber $m(y)$ take maximum and minimum values, respectively. The value of $\bar{R}(0)$ calculated from (49) for experiments 1–12 varies in the range $O(10^{-1})$–$O(2)$, with values in excess of one being obtained for experiments 3, 4, 7 and 8. Hence, the momentum flux into the sidewall boundary layers is expected to be less than, or comparable to, the vertical momentum flux in the vicinity of the tank bottom. Even in experiments 3, 4, 7 and 8, however, the neglect of the sidewall boundary layers may be justified on the basis that dissipation in the lower portion of the tank is very weak in absolute terms (see observations in figure 4(*a*) and prediction in figure 17). The rate at which horizontal momentum decreases with height increases as the vertical advection $V(y)$ decreases. Thus, the absolute dissipation in the upper portion of the tank is greater because the residence time of fluid there is greater. In addition the dissipation in the upper portion of the tank is due primarily to the vertical flux of horizontal momentum since $\bar{R}(y) \ll 1$ there. As $y$ increases, $m(y)$ increases and $V(y)$ decreases: by (49) $\bar{R}(y)/\bar{R}(0) \approx 0.5$ at $y = 0.25$ and $\bar{R}(y)/\bar{R}(0) < 0.2$ by $y = 0.5$.

## REFERENCES

Baines, W. D. & Turner, J. S. 1969 Turbulent buoyant convection from a source in a confined region. *J. Fluid Mech.* **37**, 51–80.

Batchelor, G. K. 1967 *An Introduction to Fluid Dynamics*. Cambridge University Press.

Bretherton, F. P. 1967 The time-dependent motion due to a cylinder moving in an unbounded rotating or stratified fluid. *J. Fluid Mech.* **28**, 545–570.

Cooper, P. & Linden, P. F. 1996 Natural ventilation of an enclosure containing two buoyancy sources. *J. Fluid Mech.* **311**, 153–176.

Gill, A. E. 1982 *Atmosphere-Ocean Dynamics*. Academic.

Germeles, A. E. 1975 Forced plumes and mixing of liquids in tanks. *J. Fluid Mech.* **71**, 601–623.

Imberger, J., Thompson, R. & Fandry, C. 1976 Selective withdrawal from a finite rectangular tank. *J. Fluid Mech.* **78**, 489–512.

Killworth, P. D. 1977 Mixing on the Weddell Sea continental slope. *Deep-Sea Res.* **24**, 427–448.

Killworth, P. D. & Turner, J. S. 1982 Plumes with time-varying buoyancy in a confined region. *Geophys. Astrophys. Fluid Dyn.* **20**, 265–291.

Lighthill, J. 1978 *Waves in Fluids*. Cambridge University Press.

Linden, P. F. & Cooper, P. 1996 Multiple sources of buoyancy in a naturally ventilated enclosure. *J. Fluid Mech.* **311**, 177–192.

Manins, P. C. 1976 Intrusion into a stratified fluid. *J. Fluid Mech.* **74**, 547–560.

Manins, P. C. 1979 Turbulent buoyant convection from a source in a confined region. *J. Fluid Mech.* **91**, 765–781.

Martin, S. & Long, R. R. 1968 The slow motion of a flat plate in a viscous stratified fluid. *J. Fluid Mech.* **31**, 669–688.

Morton, B. R., Taylor, G. I. & Turner, J. S. 1956 Turbulent gravitational convection from maintained and instantaneous sources. *Proc. R. Soc. Lond.* A **234**, 1–23.

Ruddick, B. R. & Shirtcliffe, T. G. L. 1979 Data for double diffusers: physical properties of aqueous salt-sugar solutions. *Deep-Sea Res.* **26**, 775–787.

Turner, J. S. 1973 *Buoyancy Effects in Fluids*. Cambridge University Press.

Turner, J. S. 1980 Differentiation and layering in magma chambers. *Nature* **285**, 213–215.

Turner, J. S. 1986 Turbulent entrainment: the development of the entrainment assumption, and its application to geophysical flows. *J. Fluid Mech.* **173**, 431–471.

Turner, J. S. 1997 G. I. Taylor in his later years. *Ann. Rev. Fluid Mech.* **29**, 1–25.

Worster, M. G. & Huppert, H. E. 1982 Time-dependent density profiles in a filling box. *J. Fluid Mech.* **132**, 457–466.